Final Report for the NERI Project

DE-FC07-05ID14651

University of Michigan

Development of TRU Transmuters for Optimization of the Global Fuel Cycle

Principal Investigator: John C. Lee

Period of Performance: April 1, 2005 – December 31, 2008

Date of Report: March 31, 2009

Final Report for the NERI Project

Development of TRU Transmuters for Optimization of the Global Fuel Cycle

April 1, 2005 – December 31, 2008

John C. Lee and Ronald F. Fleming
University of Michigan

This final report summarizes the research activities during the entire performance period of the NERI grant, including the extra 9 months granted under a no-cost time extension. Building up on the 14 quarterly reports submitted through October 2008, we present here an overview of the research accomplishments under the five tasks originally proposed in July 2004, together with citations for publications resulting from the project. Since the last quarterly report dated October 31, 2008, one paper has been accepted for presentation at the next American Nuclear Society (ANS) Conference in June 2009. Following the review of the summary of the paper, the ANS Division of Fuel Cycle and Waste Management invited us to submit a full paper, which we have prepared, for publication in a special issue of *Nuclear Technology*. In addition, we have recently prepared for publication in *Nuclear Science and Engineering* a manuscript summarizing the fuel cycle optimization algorithms for the sodium-cooled fast reactor (SFR) developed under the grant. These three latest papers are attached to the report.

1. Summary of research accomplishments

Task 1. Optimization of fast rector transmuter

With the objective to perform systematic optimization of SFR transmuters, we developed a general fuel cycle optimization methodology that could be applied to the optimization of fuel cycles both for SFRs and pressurized water reactors (PWRs). The key features of the optimization algorithms include:

(1) The optimization algorithms are based on the calculus of variations that allows for a systematic augmentation of desired objective function typically expressed in terms of end-of-cycle (EOC) fuel cycle attributes,
(2)The Lagrange multipliers introduced in the augmentation process allows for direct representation of system constraints, e.g., the power peaking factor constraint,
(3) A first-order variation of the augmented objective function yields the necessary condition for optimality together with Euler-Lagrange equations for the Lagrange multipliers cast in the form of adjoint system equations,
(4) The adjoint flux and depletion equations are solved backward from EOC to beginning-of-cycle (BOC), with discontinuities introduced in the adjoint neutron flux at the constraint boundaries,
(5) The adjoint flux, combined with the forward flux, provides the search directions for the control variables, e.g., transuranics (TRU) enrichment or burnable absorber (BA) placement, and
(6) The combination of forward diffusion-depletion calculations and backward adjoint flux-depletion calculations is repeated until the objective function is minimized.

The deterministic algorithms may be initiated from arbitrary core configurations and typically converge in a few iterations to yield optimal configurations desired. This is to be contrasted with many of the popular stochastic optimization algorithms that require

10^4~10^5 iterations before an optimal configuration is attained. Furthermore, through a separate backward diffusion theory algorithm, the power peaking constraints are rigorously satisfied. The optimization algorithm for SFR transmuter cases systematically yields an optimized core configuration with a reduced power peaking factor and lower reactivity swing over a fuel cycle. Similarly, the PWR optimization algorithm applied to the AP600 design yields a lower radial peaking factor than that presented in the Standard Safety Analysis Report, together with a reduced number of BA rods required. This implies that the improved design allows for (a) a higher power density, (b) an increased cycle length due to a reduction in the residual BA penalty at EOC, and (c) savings in the BA cost. Two doctoral dissertations were completed under Task 1.

Publications resulting from Task 1 are listed below:

1. R. T. Sorensen, J. C. Davis, and J. C. Lee, "Systematic Method for Optimizing Plutonium Transmutation in LWRs," *Trans. Am. Nucl. Soc*., *95*, 217 (2006).

2. J. C. Lee, J. C. Davis, and R. T. Sorensen, "TRU Transmuters for Nuclear Fuel Cycle Optimization," Poster presentation, Computational Engineering and Science Conference, Washington DC (April 2007).

3. J. C. Davis and J. C. Lee, "Optimizing SFR Transmutation Through Direct Adjoining Control Theory," *Trans. Am. Nucl. Soc*., *97*, 96 (2007).

4. J. C. Davis, N. W. Touran, and J. C. Lee, "SFR Fuel Cycle Optimization Using Direct Adjoining Control Theory," to be submitted for publication in *Nucl. Sci. Eng.* (attachment 1).

Task 2. Development of equilibrium cycle method for PWR configurations

As part of the overall effort of the project to optimize the global nuclear fuel cycle, we developed a systematic search methodology for equilibrium cycle configurations in PWRs. In few-group macroscopic fuel depletion calculations typically performed for PWR fuel cycle analyses, equilibrium cycle configurations would require repetitive transition fuel cycle calculations slowly approaching an asymptotic configuration. To expedite the approach to an equilibrium cycle, we developed a method that extracts few-group microscopic reaction rates from lattice physics calculations, which may then be used to arrive at an approximate asymptotic configuration. Through the use of microscopic reactions rates, we are able to arrive at a balanced excore cycle for each set of lattice physics calculations and the corresponding macroscopic cross section libraries. Once the excore nuclide balance is satisfied, we perform a new set of CPM-3 calculations to update the microscopic reaction rates. This process is repeated for a fixed fuel loading pattern to arrive at an equilibrium cycle, resulting in a significant reduction in the number of repetitive lattice-physics depletion calculations required for convergence to an equilibrium cycle. We developed the equilibrium cycle methodology for both assembly-level calculations, via a linear reactivity model, and global 3-D diffusion theory calculations.

Publications resulting from Task 2 are listed below:

1. R. T. Sorensen and J. C. Lee, "LWR Equilibrium Cycle Search Methodology for Global Fuel Cycle Analysis," *Trans. Am. Nucl. Soc*., *93*, 622 (2005).

2. R. T. Sorensen and J. C. Lee, "LWR Equilibrium Cycle Search Methodology for Assembly-Level Fuel Cycle Analysis," *Nucl. Sci. Eng.*, *158*, 213 (2008).

3. W. R. Morgan and J. C. Lee, "Development of a 3-D Global Equilibrium Cycle Methodology for PWRs," accepted for presentation at the American Nuclear Society Conference in June, 2009 (attachment 2).

4. W. R. Morgan and J. C. Lee, "3-D Global Equilibrium Cycle Methodology for PWRs," to be submitted for publication in *Nucl. Technol.* (invited, attachment 3).

Task 3. Evaluation of diverse fuel cycle options with DANESS

This task was proposed with the intention of utilizing the dynamic fuel cycle modeling code DANESS under development at Argonne National Laboratory. After some experimentation with DANESS, it was decided to use a new fuel cycle code, VISION, emerging from Idaho National Laboratory. Based on the database for various fuel cycles incorporated into the VISION code package and VISION calculations using the Powersim software, an Excel-based script, Equilibrium Operation Fuel Cycle Model (EO-FCM), was developed for efficient fuel cycle calculations. EO-FCM provides a simple calculation of key fuel cycle parameters for a nuclear park scenario consisting of up to two reactor types operating in equilibrium operation (EO) mode and approximating the detailed inventory tracking in transitional operation (TO) mode employed by the dynamic fuel cycle modeling codes. EO-FCM models a fuel cycle campaign, yielding end-of-scenario (EOS) inventories of used nuclear fuel (UNF), heavy metal (HM) reprocessed, fuel cycle economics and electricity produced. The EO-FCM module accurately tracks more complex TO calculations performed with VISION and provides, in a simple efficient manner, valuable physical insights into key characteristics of diverse fuel cycles. One M.S. thesis was completed under the task.

One publication resulted from Task 3:

J. Haas and J. C. Lee, "Equilibrium Transuranic Management Scheme for Diverse Fuel Cycle Analysis," *Proc. International Conference on Reactor Physics, Nuclear Power: A Sustainable Resource*, Interlaken, Switzerland (2008).

Task 4. Optimization of global fuel cycle

During the early phase of the grant, substantial effort was made for this task concentrating on the use of thorium in the transmuters both for the PWR and SFR configurations. The Th-based mixed oxide (TMOX) design, comprising (Th-Pu)O_2 and (Th-^{233}U) fuel rods in a heterogeneous PWR fuel assembly configuration, would achieve a 95% destruction of the ^{239}Pu and a 70% consumption of the total Pu in once-through cycles. Two-tier transmutation systems featuring a synergistic combination of PWR and SFR cycles were also studied, where minor actinides (MAs) from PWR UNF are reprocessed and recycled in the form of (Th-TRU)-Zr metallic fuel for efficient consumption of MAs. As the research program for the project progressed, the emphasis for the global fuel cycle optimization shifted gradually to the development of fuel cycle optimization methods culminating in two doctoral dissertations, as discussed in Task 1.

Publications resulting from Task 2 are listed below:

1. R. T. Sorensen, J. C. Davis, and J. C. Lee, "Thorium-based Fuels for Enhancing Plutonium Transmutation in Light Water Reactors," *Trans. Am. Nucl. Soc*., *94*, 87 (2006).

2. J. C. Davis, R. T. Sorensen, J. C. Lee, and R. F. Fleming, "Transmutation Characteristics of Thorium-Based Fuel in a Multiple-Tier Fuel Cycle," *Trans. Am. Nucl. Soc*., *94*, 89 (2006).

Task 5. Development of simplified fuel cycle model

The original intent for this task was to develop semi-analytic models for simplified dynamic fuel cycle analyses in parallel with the DANESS code discussed under Task 3. The simple analytic models we studied, however, revealed significant limitations when applied to realistic fuel cycles involving TRU transmutations. With the development of the VISION software at Idaho National Laboratory, our interest and focus shifted to VISION, which eventually resulted in developing the EO-FCM script discussed under Task 3.

2. Undergraduate and Graduate Student Participation

During the course of the grant, two undergraduate students and 10 graduate students participated in the project:

Undergraduate students: Anree Little and Josh Miesel

M.S. students: Natallia Pinchuk, Jason R. Haas, William R. Morgan, Adam Hoffmann, Stephen Rice, and Fariz A. Rahman

Ph.D. students: Reuben T. Sorensen, Jeffrey C. Davis, Nicholas W. Touran, and Yan Cao (limited).

Two Ph.D. dissertations and one M.S. thesis resulted from the project:

R. T. Sorensen, “Systematic Method for Optimizing Plutonium Transmutation in LWRs,” PhD dissertation (2006).

J. C. Davis, “Optimizing SFR Transmutation Performance through Direct Adjoining Control Theory,” PhD dissertation (2007).

J. R. Haas, “Equilibrium Transuranic Management Scheme for Diverse Fuel Cycle Analysis,” M.S. thesis (2007).

3. Concluding remarks

The AFCI-NERI project provided excellent support for two undergraduate and 10 graduates students at the University of Michigan during a period of three years and nine months. Significant developments were achieved in three areas:

(1) Efficient deterministic fuel cycle optimization algorithms both for PWR and SFR configurations,

(2) Efficient search algorithm for PWR equilibrium cycles, and
(3) Simplified Excel-based script for dynamic fuel cycle analysis of diverse cycles.

The project resulted in a total of 8 conference papers and three journal papers, including two that will be submitted shortly. Another journal paper summarizing the PWR fuel cycle optimization methodology is under preparation and will be submitted during the summer.

List of Attachments

1. J. C. Davis, N. W. Touran, and J. C. Lee, "SFR Fuel Cycle Optimization Using Direct Adjoining Control Theory," to be submitted for publication in *Nucl. Sci. Eng.*

2. W. R. Morgan and J. C. Lee, "Development of a 3-D Global Equilibrium Cycle Methodology for PWRs," summary of a paper to be presented at the ANS meeting, June 2009.

3. W. R. Morgan and J. C. Lee, "3-D Global Equilibrium Cycle Methodology for PWRs," to be submitted for publication in *Nucl. Technol.*

SFR Fuel Cycle Optimization Using Direct Adjoining Control Theory

Jeffrey C. Davis, Nicholas W. Touran, and John C. Lee

Department of Nuclear Engineering and Radiological Sciences
University of Michigan, Ann Arbor, MI 49109-2104

Corresponding author: Nicholas W. Touran

Mailing Address: Department of Nuclear Engineering and Radiological Sciences
University of Michigan
2355 Bonisteel Blvd.
Ann Arbor, MI 48109-2104

Tel: (734) 272-2670
Fax: (734) 763-4540
Email: ntouran@umich.edu

Total number of pages: 43
Number of tables: 2
Number of figures: 13

Abstract

An optimal control method has been developed in multi-group, 3-D, diffusion-depletion state-space simulations to optimize the loading patterns of fast reactors. Given an objective function, a generalized Kuhn-Tucker theorem produces necessary conditions for optimality in the form of Euler-Lagrange equations, terminal conditions, and optimality conditions while directly accounting for the power-peaking inequality constraint. The terminal conditions require the Euler-Lagrange system be solved backwards in time, from end of cycle to beginning of cycle, while the inequality constraint introduces discontinuities into the Lagrange multipliers at the junction points. The possible inequality constraint violations that arise throughout the cycle when the optimality conditions cannot be explicitly satisfied are eliminated by backwards diffusion theory. The method has been applied to minimize the reactivity swing objective function in three similar metal-fueled, sodium-cooled transuranic burner reactor systems. In a typical case, the method has reduced the reactivity swing from 4.0% to 2.5% while bringing the hot channel factor F_q from 3.0 to 2.0 in a single iteration.

I. INTRODUCTION

Many aspects of the performance of any nuclear reactor depend pivotally on the fuel loading pattern. The optimization of the pattern is of fundamental interest to fuel designers, as approaching the optimal pattern allows cycle length, power peaking, reactivity swing, coefficients of reactivity, and transmutation characteristics to be such that the reactor operates as safely and as economically as possible. The art of optimizing reactor fuel patterns was historically performed manually, guided by designer experience and heuristics. More recently, automated tools have been developed to help designers quickly and systematically reach optimal or near-optimal loading patterns.

Automatic optimization tools fall into two general categories – deterministic and stochastic. Early optimization methodologies were generally deterministic due to the computational efficiency of this category. Tzanos et al.[1] developed a method to optimize the distribution of material in a one-dimensional infinite cylinder with respect to integral parameters by linearizing the diffusion equation and power equation with a Taylor series expansion and then using a linear programming algorithm to find an optimal solution. The method considered power peaking constraints, but only works for optimal controls that are close to the original control.

Terney and Williamson[2] invoked Pontryagin's maximum principle to deterministically optimize reload cores. They minimized power peaking by augmenting the diffusion, power normalization, and burnup equations to a cost functional with Lagrange multipliers. Forcing first-order variations of the functional to vanish, they derived Euler-Lagrange equations which they solved backwards in time from end-of-cycle (EOC) to beginning-of-cycle (BOC) to obtain a reload pattern.

Following Terney and Williamson, Drumm and Lee[3] applied the Pontryagin maximum principle to a LWR cycle-length extension problem, using penalty functions to maintain power-peaking compliance. The method effectively extended the cycle length, but was inefficient at satisfying the power-peaking constraint at all times during the cycle.

Building on these experiences, Wu[4] solved a similar cycle-length extension problem by directly adjoining the power-peaking constraint to the cost functional, an approach developed by Jacobson, et al.[5]. The one-group, one-dimensional formulation used the solution of the Euler-Lagrange equations to reach an optimal gadolinium loading in fuel, uniformly distributed axially, implementing the conjugate gradients search-direction updated method for efficiency. Wu was able to account for constraint violations throughout the cycle in a somewhat ad hoc manner.

Sorensen[6] applied Wu's formulation to two-dimensional, two-group diffusion theory, implementing backwards diffusion theory (BDT) developed by Crowther[7] to account for mid-cycle power peaking violations. This involved solving the diffusion equation backwards to obtain burnable poison distributions, given the desired optimal flux shape. Sorensen applied this approach to a PWR system, using the method of conjugate gradients to update the state, Euler-Lagrange, and optimality conditions while satisfying the power peaking constraint throughout the cycle.

Stochastic methods of optimizing loading patterns have emerged with the massive improvements in computational performance throughout the last few decades. These methods use concepts developed for artificial intelligence, attempting to learn how to load reactors based on repeated tests of stimulation and reaction. The two most popular stochastic methods have become genetic algorithms and simulated annealing algorithms. Jessee and Kropaczek [8] used simulated annealing to optimize boiling water reactor loadings, control rod programs, and gadolinium distributions, creating an abstract nuclear reactor analogy to a solid material slowly cooling to its lowest energy state. The inequality constraint is accounted for with a penalty function. A given reactor state is perturbed randomly, giving a new objective function value. If the new value is lower than the previous, the perturbation is accepted. If not, it is only accepted if a random number exceeds the Boltzmann factor. When the reactor reaches a "frozen" state, it is considered optimal.

Dechaine and Feltus[9, 10] developed a genetic algorithm methodology that uses bio-

logical evolution to reach optimal loading patterns. In this method, an initial population of several hundred loading patterns are combined imperfectly into a second generation of offspring loading patterns. The offspring patterns undergo various genetic operations such as crossover and random mutation, eventually generating an optimal offspring as judged by the objective functional, which is calculated for every pattern. Power peaking is again accounted for with a penalty function.

Both categories present advantages and shortcomings. The global nature of the stochastic philosophy better handles multi-objective problems, but the algorithms require hundreds of thousands of loading pattern tests to ascertain optimality. When evaluating equilibrium fuel cycles, the sheer volume of calculations needed to perform stochastic algorithms becomes impractical to implement. Jacobson and Lele[11] have shown that the indirect method of accounting for inequality constraints with penalty functions leads to numerical difficulties and the inability to find optimal solutions. Considering this, and that penalty methods may lead to middle-of-cycle constraint violations, we prefer the direct adjoining treatment. Thus, for efficiency and the ability to use a rigorous power-peaking inequality, we have chosen a deterministic method.

In this paper, we present the derivation and application of a direct adjoining optimal control method based on the generalized Kuhn-Tucker theorem for designing fuel enrichment and burnable poison loading patterns in a sodium-cooled fast reactor. We extend the time-domain theory based on ordinary differential equations to a space-time domain described by partial differential equations, where control may only be specified at BOC. The formulation solves the multi-group, 3D, quasi-static state-equations of the reactor along with the corresponding Euler-Lagrange equations containing a directly adjoined power-peaking state constraint to arrive at a control satisfying necessary conditions for optimality, while guaranteeing compliance with power-peaking requirements throughout the cycle with backwards diffusion theory. The derivation of the Euler-Lagrange equations from variational calculus concepts is presented in Sec. II., with discussion of several subtleties. The application of the equations to a reactor simulator is discussed in Sec.

III. Results from this application are presented and discussed in Sec. IV., followed by our summary and conclusions of this work in Sec. V.

II. DERIVATION OF THE ADJOINING CONTROL METHOD

In this section, we begin with the formulation of the state equations of a SFR system. We then introduce the cost functional to be optimized considering an adjoined inequality state constrained. We derive necessary conditions for optimality, which are captured by the Euler-Lagrange equations, terminal conditions, jump conditions, and a Hamiltonian minimization condition.

II.A. State Equations of a SFR System

The *state* of a system is the smallest set of information specified at time $t = t_0$ that is sufficient to predict the behavior of the system at later times[12]. We wish to model the power and reactivity of a dynamic nuclear reactor, considering only the characteristic time scales of fuel burnup. Thus, neutron flux and nuclide number densities are required as functions of space and time. We will neglect thermal hydraulic feedback for simplicity, while conceding that it should be considered in a full-system design optimization procedure.

Since we expect the neutron flux will vary slowly in time, we represent its time dependence in a quasi-static fashion, solving the multi-group Bateman equation for nuclide densities at various time-steps while assuming constant flux between them:

$$\frac{\partial N_i}{\partial t} = -N_i \left[\sum_{g=1}^{G} \sigma_{ag,i} \phi_g + \lambda_i \right] + \sum_{j=1}^{I} N_j \left[\left(\sum_{g=1}^{G} \gamma_{g,,j \to i} \phi_g \right) + \lambda_{j \to i} \right], \tag{1}$$

where

$\sigma_{ag,i}$ is the g-th group absorption cross section for nuclide i,

λ_i is the decay constant for nuclide i,

$\gamma_{g,,j\to i}$ is the transmutation yield from nuclide j to nuclide i, and

$\lambda_{j\to i}$ is the decay constant from nuclide j to nuclide i.

We can represent in matrix notation as:

$$\frac{\partial N}{\partial t} = AN, \tag{2}$$

where A is the burn matrix, containing all the reaction rates of transmutation and decay. As the problem is quasi-static, the neutron flux will be temporally flat between time step boundaries, with jump discontinuities at each one. To describe the shape of the neutron flux, we assume the global-diffusion approach and employ both the steady-state, 3-D, multi-group diffusion equation and the multi-group Fick's law for a system of G energy groups:

$$\nabla \cdot J + M\phi = \frac{1}{k}\chi F^T \phi, \text{ and} \tag{3}$$

$$\nabla\phi = -D^{-1}J, \tag{4}$$

where we have used the standard notation. J is the neutron current, ϕ is the neutron flux, M is a GxG matrix consisting of removal and in-scattering cross sections, k is the dominant eigenvalue, χ is a vector of length G containing the fission neutron energy distribution, F is a vector of length G containing fission neutron yields, and D is a diagonal GxG matrix consisting of diffusion coefficients. Solving these two coupled equations at each time step will fully define the spatial shape and energy structure of the neutron flux. The magnitude of the flux is uniquely determined by setting a specific power level for the reactor and using the power normalization volume integral:

$$P(t) = \int_V d\mathbf{r}\, p(\mathbf{r},t) = \int_V d\mathbf{r} \sum_{g=1}^{G} \kappa\Sigma_{f,g}\phi_g = \int_V d\mathbf{r}\, W^T\phi, \tag{5}$$

where V represents the full volume of the reactor.

In general time-domain state-space analysis, the state of a dynamic system is presented

as a system of coupled first-order differential equations in the form:

$$\frac{\partial x}{\partial t} = f, \tag{6}$$

where x is the state vector and f contains the state equations. Modeling the behavior of our problem requires a system of partial differential equations, and we make an effort to represent it in a form analogous to that of Eq. (6). Nothing need be done to the diffusion equation nor to Fick's law to comply with this practice, as they are both first-order differential equations in neutron current and neutron flux respectively. However, the power normalization integral requires some transformation. For a 3-D problem, we break the integral normalization equation into three related first-order differential equations by defining q, q_1, and q_2 as spatial integrals over arbitrary orthogonal directions ξ, η, and ζ.

$$q_2 = \int_0^{\xi} d\xi' W^T \phi, \tag{7}$$

$$q_1 = \int_0^{\eta} d\eta' q_2, \text{ and} \tag{8}$$

$$q = \int_0^{\zeta} d\zeta' q_1. \tag{9}$$

With these defined, we can use their differential forms as state equations.

$$\frac{\partial q}{\partial \zeta} = q_1, \tag{10}$$

$$\frac{\partial q_1}{\partial \eta} = q_2, \text{ and} \tag{11}$$

$$\frac{\partial q_2}{\partial \xi} = P(\xi, \eta, \zeta) = W^T \phi. \tag{12}$$

Finally, we have fully defined the state of the system we are interested in modeling with a coupled system of first order differential equations. These are known as the state-

equations, and are concisely:

$$\begin{bmatrix} \nabla\phi \\ \nabla \cdot J \\ \frac{\partial q}{\partial \xi} \\ \frac{\partial q_1}{\partial \eta} \\ \frac{\partial q_2}{\partial \zeta} \\ \frac{\partial N}{\partial t} \end{bmatrix} = \begin{bmatrix} -D^{-1}J \\ \left(k^{-1}B - M\right)\phi \\ q_1 \\ q_2 \\ W^T\phi \\ AN \end{bmatrix}, \text{ or} \tag{13}$$

$$\mathbb{D}x = f, \tag{14}$$

where we introduced a total derivative operator $\mathbb{D}$, which we define as:

$$\mathbb{D} \equiv \begin{bmatrix} \nabla & & & & & & \\ & \nabla\cdot & & & & & \\ & & \frac{\partial}{\partial\xi} & & & & \\ & & & \frac{\partial}{\partial\eta} & & & \\ & & & & \frac{\partial}{\partial\zeta} & & \\ & & & & & \frac{\partial}{\partial t} & \end{bmatrix}. \tag{15}$$

To meet standard design safety requirements, any the reactor state must satisfy power-peaking requirements at all times. The maximum power of any region of the reactor core must not exceed the core-average power multiplied by a specified peaking factor. To comply with this requirement, we apply a power-peaking inequality state constraint to the system.

$$S = W^T\phi(\mathbf{r}, t) - p_{max} \leq 0. \tag{16}$$

With our state system in this form, we can apply optimal control theory using the calculus of variations, taking special care to satisfy the inequality constraint.

II.B. The Augmented Objective Functional and Euler-Lagrange Equations

Before we begin the optimization process, we must choose a performance index Φ that somehow measures the characteristics that we are interested in minimizing. For typical reactor design purposes, this may be the reactivity swing or the transuranic destruction during a cycle. Then, the cost functional to minimize has the form:

$$K = \int_V d\mathbf{r}\, \Phi(\mathbf{r}, \tau). \tag{17}$$

We seek the optimal control u^* out of the set of all possible controls that guides the reactor from its initial state $x(0)$ to a final state $x(\tau)$ in a manner that minimizes K while satisfying the power-peaking inequality constraint.

We approach this problem statement by augmenting K with the state equations using a vector of scalar multiples, λ, which are familiar from vector calculus as Lagrange multipliers, often used to solve constrained systems of equations. For the inequality constraint, we follow the same process with an additional scalar Lagrange multiplier, $\overline{\eta}$:

$$K^\dagger = \int_V d\mathbf{r}\, \Phi(\mathbf{r}, \tau) + \int_V d\mathbf{r} \int_0^\tau dt \left[\lambda^T (f - \mathbb{D}x) + S\overline{\eta}\right]. \tag{18}$$

By forcing first-order perturbations in this functional to disappear with respect to the state variables and to the control, we derive conditions necessary for a stationary $K^\dagger$, which are in turn necessary conditions for optimality. Since this problem is quasi-static, we separate the time-dependent state variables from the time-independent variables in this representation by introducing the sub-vectors x_t and $x_s$and their corresponding derivative operators, $\frac{\partial}{\partial t}$ and $\mathbb{D}_s$. Under this separation, the augmented function is:

$$K^\dagger = \int_V d\mathbf{r}\, \Phi(\mathbf{r}, \tau) + \int_V d\mathbf{r} \int_0^\tau dt \left[\lambda_s^T (f_s - \mathbb{D}_s x_s) + \lambda_t \left(f_t - \frac{\partial}{\partial t} x_t\right) + S\overline{\eta}\right]. \tag{19}$$

We introduce first-order perturbations here, following the generalized Kuhn-Tucker theorem:

$$\begin{aligned}
\delta K^{\dagger} &= \int_V d\mathbf{r} \left\{ \left[\frac{\partial \Phi\left(\mathbf{r},\tau\right)}{\partial x_s} \right]^T \delta x_s\left(\mathbf{r},\tau\right) + \left[\frac{\partial \Phi\left(\mathbf{r},\tau\right)}{\partial x_t} \right]^T \delta x_t\left(\mathbf{r},\tau\right) \right\} \\
&+ \int_V d\mathbf{r} \int_0^{\tau} dt \left[\lambda_s^T \left(\frac{\partial f_s}{\partial x_s}\delta x_s + \frac{\partial f_s}{\partial u}\delta u - \mathbb{D}_s \delta x_s \right) + \overline{\eta} \left(\frac{\partial S}{\partial x_s} \right)^T \delta x_s \right] \\
&+ \int_V d\mathbf{r} \int_0^{\tau} dt \left[\lambda_t^T \left(\frac{\partial f_t}{\partial x_t}\delta x_t + \frac{\partial f_t}{\partial u}\delta u - \frac{\partial}{\partial t}\delta x_t \right) + \overline{\eta} \left(\frac{\partial S}{\partial x_t} \right)^T \delta x_t \right] = 0.
\end{aligned} \tag{20}$$

We simplify this by defining $\mathbb{D}_s^*$ as a differential operator satisfying the adjoint property:

$$\int_V d\mathbf{r} \int_0^{\tau} dt\ \lambda_s^T \mathbb{D}_s \delta x_s = \int_V d\mathbf{r} \int_0^{\tau} dt\ \left(\mathbb{D}_s^* \lambda_s\right)^T \delta x_s. \tag{21}$$

We continue simplification by integrating the temporal state variables by parts:

$$\int_V d\mathbf{r} \int_0^{\tau} dt\ \lambda_t^T \frac{\partial}{\partial t}\delta x_t = \int_V d\mathbf{r} \left[\lambda_t^T \delta x_t \big|_0^{\tau} - \int_0^{\tau} dt\ \left(\frac{\partial \lambda_t}{\partial t} \right)^T \delta x_t \right]. \tag{22}$$

Next, we collect like terms to obtain:

$$\begin{aligned}
\delta K^{\dagger} &= \int_V d\mathbf{r} \left\{ \left[\frac{\partial \Phi\left(\mathbf{r},\tau\right)}{\partial x_s} \right]^T \delta x_s\left(\mathbf{r},\tau\right) + \left[\frac{\partial \Phi\left(\mathbf{r},\tau\right)}{\partial x_t} - \lambda_t\left(r,\tau\right) \right]^T \delta x_t\left(\mathbf{r},\tau\right) \right\} \\
&+ \int_V d\mathbf{r} \int_0^{\tau} dt \left\{ \left[\left(\mathbb{D}_s^* \lambda_s\right)^T + \lambda_s^T \frac{\partial f_s}{\partial x_s} + \overline{\eta} \left(\frac{\partial S}{\partial x_s} \right)^T \right] \delta x_s \right\} \\
&+ \int_V d\mathbf{r} \int_0^{\tau} dt \left\{ \left[\left(\frac{\partial}{\partial t}\lambda_t \right)^T + \lambda_t^T \frac{\partial f_t}{\partial x_t} + \overline{\eta} \left(\frac{\partial S}{\partial x_t} \right)^T \right] \delta x_t \right\} \\
&+ \int_V d\mathbf{r} \int_0^{\tau} dt \left\{ \lambda_t^T \frac{\partial f_t}{\partial u} + \lambda_s^T \frac{\partial f_s}{\partial u}\delta u \right\} = 0,
\end{aligned} \tag{23}$$

where we have assumed $\delta x_t\left(\mathbf{r},0\right)$ is zero. This assumption is consistent with our model as the state of a nuclear reactor will be constant at beginning of cycle in all fuel cycle analyses. All the spatial and temporal state and Lagrange sub-vectors can be recombined

except those in the first integral:

$$\begin{aligned}
\delta K^{\dagger} &= \int_V d\mathbf{r} \left\{ \left[\frac{\partial \Phi(\mathbf{r},\tau)}{\partial x_s} \right]^T \delta x_s(\mathbf{r},\tau) + \left[\frac{\partial \Phi(\mathbf{r},\tau)}{\partial x_t} - \lambda_t(r,\tau) \right]^T \delta x_t(\mathbf{r},\tau) \right\} \\
&+ \int_V d\mathbf{r} \int_0^{\tau} dt \left\{ \left[(\mathbb{D}^* \lambda)^T + \lambda^T \frac{\partial f}{\partial x} + \overline{\eta} \left(\frac{\partial S}{\partial x} \right)^T \right] \delta x \right\} \qquad (24) \\
&+ \int_V d\mathbf{r} \int_0^{\tau} dt \left\{ \lambda^T \frac{\partial f}{\partial u} \delta u \right\} = 0.
\end{aligned}$$

To force first-order perturbations to vanish, we set each integrand to zero. Forcing terms involving δx_t to vanish provides terminal conditions on the temporal Lagrange multipliers:

$$\frac{\partial \Phi(\mathbf{r},\tau)}{\partial x_t} = \lambda_t(r,\tau). \qquad (25)$$

This condition requires that we solve the temporal Lagrange multipliers backwards in time, from EOC to BOC.

We restrict the objective function to be an explicit function of x_t, and thus the terminal variations in x_s become inconsequential, as:

$$\frac{\partial \Phi(\mathbf{r},\tau)}{\partial x_s} = 0. \qquad (26)$$

This restriction limits our possible objective functions to global parameters, and eliminates the possibility of optimizing with any spatial resolution, such as maximizing TRU destruction in a particular location of the core. If such detailed optimization is desired, this restriction could be relaxed with the additional condition that:

$$\left(\frac{\partial \Phi(\mathbf{r},\tau)}{\partial x_s} \right)^T \delta x_s(\mathbf{r},\tau) = 0, \qquad (27)$$

thus eliminating the limitation. We arrive at the Euler-Lagrange (E-L) equations by

forcing the terms involving δx to vanish in Eq. (24):

$$\mathbb{D}^{*}\lambda = -\left(\frac{\partial f}{\partial x}\right)^{T}\lambda - \frac{\partial S}{\partial x}\overline{\eta}. \tag{28}$$

The Jacobian of f can be expanded as

$$\left(\frac{\partial f}{\partial x}\right)^{T} = \begin{bmatrix} 0 & \left(k^{-1}B - M\right)^{T} & 0 & 0 & W & \left(\frac{\partial}{\partial \phi}AN\right)^{T} \\ \left(-D^{-1}\right)^{T} & 0 & 0 & 0 & 0 & 0 \\ 0 & 0 & 0 & 0 & 0 & 0 \\ 0 & 0 & 1 & 0 & 0 & 0 \\ 0 & 0 & 0 & 1 & 0 & 0 \\ 0 & \left\{\frac{\partial}{\partial N}\left[\left(k^{-1}B - M\right)\phi\right]\right\}^{T} & 0 & 0 & \left(\frac{\partial}{\partial N}W^{T}\phi\right)^{T} & A^{T} \end{bmatrix}, \tag{29}$$

and the state-vector derivative of the constraint is:

$$\frac{\partial S}{\partial x} = \begin{bmatrix} \frac{\partial}{\partial \phi}W^{T}\phi \\ 0 \\ 0 \\ 0 \\ 0 \\ \frac{\partial}{\partial N}W^{T}\phi \end{bmatrix} = \begin{bmatrix} W \\ 0 \\ 0 \\ 0 \\ 0 \\ \frac{\partial}{\partial N}W^{T}\phi \end{bmatrix}. \tag{30}$$

With these terms identified, we can simplify the E-L equations to:

$$\nabla \cdot \lambda_1 = -\left(k^{-1}B - M\right)\lambda_2 - W\lambda_5 - \left(\frac{\partial}{\partial \phi}AN\right)^{T}\lambda_6 - W\overline{\eta}, \tag{31}$$

$$\nabla \lambda_2 = \left(D^{-1}\right)^{T}\lambda_1, \text{ and} \tag{32}$$

$$\frac{\partial}{\partial t}\lambda_6 = -\left\{\frac{\partial}{\partial N}\left[\left(k^{-1}B - M\right)\phi\right]\right\}^{T}\lambda_2 - \left(\frac{\partial}{\partial N}W^{T}\phi\right)^{T}\left(\lambda_5 + \overline{\eta}\right) - A^{T}\lambda_6. \tag{33}$$

Brief observation provides reason to redefine the Lagrange multipliers after their state-

space analogs, which in turn justifies enumerating the E-L equations as the adjoint diffusion equation, the adjoint Fick's law, and the adjoint depletion equation, yielding:

$$\begin{bmatrix} \lambda_1 \\ \lambda_2 \\ \lambda_3 \\ \lambda_4 \\ \lambda_5 \\ \lambda_6 \end{bmatrix} = \begin{bmatrix} -J^* \\ \phi^* \\ q_2^* \\ q_1^* \\ q^* \\ N^* \end{bmatrix}, \tag{34}$$

where we have listed the adjoint current vector, the adjoint flux, the three adjoint power components, and the adjoint number density. This identification is done for notational convenience, and does not imply that the adjoint variables behave similarly to their state-space analogs, but only that they are related though equations of similar form. For example, we allow negative adjoint flux and adjoint number densities – concepts that are meaningless in state-space.

The term in the perturbed functional $K^\dagger$ involving perturbations in the control variable, u, provides the optimality condition which we will use to find the optimal control. Borrowing from classical mechanics, we define the Hamiltonian of the system as:

$$H = \lambda^T f + \overline{\eta} S, \tag{35}$$

and obtain:

$$\int_V d\mathbf{r} \int_0^\tau \lambda^T \frac{\partial f}{\partial u} \delta u\,(r) = \int_V d\mathbf{r} \int_0^\tau \frac{\partial H}{\partial u} = 0. \tag{36}$$

We again set the integrand to zero to ensure this is met:

$$\frac{\partial H}{\partial u} = 0. \tag{37}$$

Our task becomes solving the E-L equations (which require the real flux, power, and

number densities to be known) and using the results in the optimality condition, from which we will be able to gain information about how to adjust the control variable to obtain a new system state that minimizes our objective function while satisfying the inequality constraint. Several subtleties must be dealt with before we can begin solving the E-L equations, including understanding the functional form of the inequality constraint multiplier, and allowing for possible jump discontinuities in the Lagrange multipliers.

II.C. The Inequality Constraint Multiplier and Jump Conditions

From the generalized Kuhn-Tucker theorem, we know that $\overline{\eta} = 0$ in the unconstrained regions and is non-decreasing, with continuous and differentiable derivatives in the constrained regions[5]. In determining the functional form of the multiplier in the constrained regions, we call an inequality constraint one of n^{th}-order if its n^{th} derivative is the first to be an explicit function of the control. In nuclear reactors, the control variable is often associated with the material cross sections. In this problem, S is a second-order inequality constraint. Thus, we expect the second derivative of the control-derivative of the Hamiltonian to also be an explicit function of the inequality multiplier, and we find a functional form for $\overline{\eta}$ in the constraint region by taking the second-derivative of the optimality condition shown in Eq. (37):

$$\nabla \cdot \nabla \left(\frac{\partial H}{\partial u} \right) = 0. \tag{38}$$

The feasibility of obtaining $\overline{\eta}$ from this equation has been discussed at length[13]. Due to the nature of $\overline{\eta}$, we must solve the E-L equations with special boundary conditions at junction points to allow for discontinuities in the adjoint variables, as discussed in App. A considering a time-domain problem. Borrowing from this discussion, we apply the jump conditions in the space-time problem, exchanging junction points in time for junction points in space.

Flux (ϕ, or x_1) is the only state variable that appears in the power-peaking inequality

constraint, so only λ_1, which we identified as $-J^*$, will undergo a jump at the j-th junction point in one of the three spatial directions

$$J^*\left(z_j^+\right) = J^*\left(z_j^-\right) + \mu_{z_j}, \tag{39}$$

where we have introduced the jump parameter from App. A. We take deliberate steps in our solution method to force these boundary conditions to be met.

II.D. The Optimality Condition

As discussed above, we find our control by setting $\frac{dH}{du} = 0$. If this optimality condition can not be met due to physical constraints, we adopt the strategy of minimizing its magnitude to approximate a stationary objective functional as best as possible. We expand our definition of H from Eq. (35) to find:

$$H = J^* D^{-1} J + \phi^{*T}\left(\frac{1}{k}B - M\right)\phi + W^T \phi q^* + N^{*T} A N + \overline{\eta}\left(W^T\phi - P_{max}\right). \tag{40}$$

If, for example, burnable poison (BP) density is the control, only absorbing terms are explicit functions of u and the condition is simply:

$$\frac{dH}{du} = -\phi^{*T}\left(\sigma_p\right)\phi = 0, \tag{41}$$

where σ_p is the microscopic absorption cross section of the poison for all terms in M that contain the poison. When transuranic enrichment is the control, then every cross section will be given by:

$$\Sigma = u\Sigma_{TRU} + (1-u)\Sigma_{non-TRU}, \tag{42}$$

where Σ_{TRU} is the summation of the macroscopic cross sections of interest of all the transuranic nuclides and $\Sigma_{non-TRU}$ follows from the summation of all the non-transuranic

nuclides. The corresponding control derivatives are:

$$\frac{\partial \Sigma}{\partial u} = \Sigma_{TRU} - \Sigma_{non-TRU}. \tag{43}$$

Number densities will also be functions of the control, in the form of:

$$N_{TRU} = uN_{TRU}^{max}, \text{ and} \tag{44}$$

$$N_{non-TRU} = (1-u)N_{non-TRU}^{max}, \tag{45}$$

where the maximum number densities are set as control limits. The control derivatives are:

$$\frac{\partial N_i}{\partial u} = \begin{cases} N_{TRU}^{max}, & N_i \text{ is a transuranic nuclide} \\ -N_{non-TRU}^{max}, & N_i \text{ is not a transuranic nuclide} \end{cases} \tag{46}$$

In this case, the control derivative of the f is:

$$f_u = \begin{bmatrix} 0 \\ \left(\frac{\nu\Sigma_f^{TRU}}{k} - \frac{\nu\Sigma_f^{non-TRU}}{k} - \Sigma_a^{TRU} + \Sigma_a^{non-TRU}\right)\phi \\ \left(\kappa\Sigma_f^{TRU} - \kappa\Sigma_f^{non-TRU}\right)\phi \\ 0 \\ 0 \\ A\overline{N} \end{bmatrix}, \tag{47}$$

where $\overline{N}$ is the nuclide density vector comprised of maximum densities for transuranic nuclides and negative maximum densities for others. This yields a more complicated optimality condition that is not shown here, but can be implemented computationally without difficulty. A more simplistic approach to TRU enrichment control is to choose ^{239}Pu number density as the control, resulting in an optimality condition similar to the BP condition, except with the opposite sign. In all cases, the Hamiltonian is a linear

function of the control. In such problems, we invoke the Pontryagin Maximum Principle, adopting bang-bang controls using $\frac{\partial H}{\partial u}$ as a switching function. Where the switching function is negative, we reduce the control, and vice versa. The magnitude of the control adjustment is determined in practice with line searches.

III. SOLUTION METHODS OF THE EULER-LAGRANGE EQUATIONS

We have modified the DIF3D 8.0 code[14] to solve the Euler-Lagrange equations as described in Sec. II. The modifications include routines to calculate the adjoint power, produce the adjoint inhomogeneous source, estimate the adjoint depletion, solve the E-L equations with the jump boundary conditions, and determine the search direction vectors. The modified executable is coupled to the REBUS-PC code[15], which provides the real number densities and flux at each time step and determines the value of the objective function. The 11-group coarse-group cross section libraries are computed by the MC**2-2 code[16] using ENDF-V data. The significant data management operations required for this coupling are performed by Python scripts[17]. A flowchart of the computational loop of calculating search directions is shown in Fig. 1.

III.A. The Adjoint Diffusion Equation

Our forward system is a critical reactor, so the adjoint diffusion equation is an inhomogeneous equation with a singular operator, and can therefore only have a unique, non-trivial solution when the Fredholm alternative is satisfied[18]. This states that if an equation of the form $A\phi = 0$ is solved, then the equation $A^*\phi^* = S^*$ can only have a non-trivial solution when the inner product $\langle \phi, S^* \rangle = 0$ or, in other words, when the adjoint source is orthogonal to the real flux.

From Eq. (31), we define the inhomogeneous source:

$$S^* \equiv W\left(q^* + \overline{\eta}\right) + \left(\frac{\partial}{\partial \phi} AN\right)^T N^*. \tag{48}$$

Before computing S^*, the form of the inequality constraint multiplier and the adjoint power must be known. We find $\overline{\eta}$ using the generalized Kuhn-Tucker theorem and then solve for q^* by forcing Fredholm alternative to be true. Thus, our adjoint source is explicitly designed so that the adjoint diffusion equation will have a unique solution.

III.A.1. Functional Form of the Inequality Constraint Multiplier

Using neutron poison number density N_p as a control, Eq. (38) becomes:

$$\begin{aligned} \nabla \cdot \nabla \left(\frac{\partial H}{\partial u}\right) &= -\nabla \cdot \nabla \left(\phi^{*T} \sigma_p \phi\right) = 0 \\ &= -\nabla \cdot \left(-D^{-1} J^{*T} \sigma_p \phi + -\phi^{*T} \sigma_p D^{-1} J\right) \\ &= D^{-1} \nabla \cdot J^{*T} \sigma_p \phi + D^{-1} J^{*T} \sigma_p \nabla \phi + \nabla \phi^{*T} \sigma_p D^{-1} J + \phi^* \sigma_p D^{-1} \nabla \cdot J. \end{aligned} \tag{49}$$

We assume flat flux on the constraint, and substitute the adjoint and forward diffusion equations for the second spatial flux derivatives, eliminating the first-order flux derivatives and leaving:

$$\begin{aligned} \nabla \cdot \nabla \left(\frac{\partial H}{\partial u}\right) &= D^{-1} \left(-M^T \phi^* + k^{-1} B^T \phi^* + W q^* + \left(\frac{\partial}{\partial \phi} AN\right)^T N^* + W \overline{\eta}\right)^T \sigma_p \phi \\ &+ \phi^{*T} \sigma_p D^{-1} \left(\frac{1}{k} B - M\right) \phi \\ &= 0, \end{aligned} \tag{50}$$

which can be simplified by integrating over energy groups:

$$q^* \sum_{g=1}^{G} W_g \sigma_{p,g} \phi_g + \sum_{g=1}^{G} \left(\phi_g^{-1} \overline{A}_g N^T\right) N^* \sigma_{p,g} \phi_g + \overline{\eta} \sum_{g=1}^{G} W_g \sigma_{p,g} \phi_g = 0, \tag{51}$$

and finally solved for $\overline{\eta}$:

$$\overline{\eta} \quad = \quad -q^* - \sum_{g=1}^{G} \left(\phi_g^{-1} \overline{A}_g N^T\right) N^* W_g^{-1}, \tag{52}$$

where $\overline{A}$ is the burn matrix without decay constants. Recall that in the unconstrained regions, $\overline{\eta} = 0$.

III.A.2. The Jump Conditions

The jumps in the adjoint current can be represented by Heaviside step functions, which have Dirac-delta function derivatives. We impose the jumps in the adjoint current by placing Dirac-delta functions in the adjoint source at the junction points where the problem switches between constrained and unconstrained. The number and locations of these jumps is computed by the forward calculation in a constraint violation-monitoring routine.

$$\overline{S}^* \equiv W\left(q^* + \overline{\eta}\right) + \left(\frac{\partial}{\partial \phi} AN\right)^T N^* + \sum_{i=0}^{N_j} \mu_j \delta\left(r - r_j\right), \tag{53}$$

where N_j is the number of jumps and μ_j is the jump parameter for the jump at r_j in one of the three hex-mesh directions. With the delta functions in place, we can integrate the adjoint diffusion equation in an ϵ-neighborhood of an arbitrary jump j in one dimension to find:

$$\int_{r_j-\epsilon}^{r_j+\epsilon} \nabla \cdot J \, dr + \int_{r_j-\epsilon}^{r_j+\epsilon} \left(M^* - k^{-1} B^*\right) \phi^* dr = \int_{r_j-\epsilon}^{r_j+\epsilon} S^* dr + \int_{r_j-\epsilon}^{r_j+\epsilon} \mu_j \delta\left(r - r_j\right) dr, \tag{54}$$

and

$$J\left(r_j^+\right) - J\left(r_j^-\right) = \mu_j, \tag{55}$$

where we see that the jump condition is indeed properly imposed. We represent the delta functions in $\overline{S}^*$ by averaging the jump parameter over the particular meshes that lie between constrained and unconstrained regions, such that the numerical integral will have

the expected results. This averaging handles jumps in any of the three spatial directions. We show the shapes of $\overline{S}^*$ and ϕ^* for a related 1-D slab problem in Fig. 2, where the spikes in the source are clearly seen.

The jump parameter varies with the magnitude of the adjoint flux almost linearly. To uniquely determine the jump parameter, we perform several simple bisection-search iterations until the normalization condition $\langle \phi, \phi^* \rangle = 1$ is satisfied for ϕ^*. We call this process the jump-parameter iteration.

III.A.3. The Adjoint Power

With $\overline{\eta}$ known and the jump conditions imposed, we apply the Fredholm alternative to solve for q^* to guarantee that the adjoint source is orthogonal to the real flux:

$$\begin{aligned}
\left\langle \phi, \overline{S}^* \right\rangle &= \left\langle \phi, W\left(q^* + \overline{\eta}\right) + \left(\frac{\partial}{\partial \phi} AN\right)^T N^* + \sum_{i=0}^{N_j} \mu_j \delta\left(r - r_j\right) \right\rangle \\
&= \langle \phi, W q^* \rangle_U - \left\langle \phi, W \left(\sum_{g=1}^{G} \phi_g^{-1} \overline{A}_g N^T N^* W_g^{-1} \right) \right\rangle_C \\
&\quad + \left\langle \phi, \left(\frac{\partial}{\partial \phi} AN\right)^T N^* \right\rangle_V + \sum_{i=0}^{N_j} \mu_j \phi_j \\
&= q^* \int_U d\mathbf{r}\, W^T \phi - \int_C d\mathbf{r}\, \left(\overline{A} N\right)^T N^* + \int_V d\mathbf{r}\, \left(\overline{A} N\right)^T N^* + \sum_{i=0}^{N_j} \mu_j \phi_j \\
&= q^* P_U + \int_U d\mathbf{r}\, \left(\overline{A} N\right)^T N^* + \sum_{i=0}^{N_j} \mu_j \phi_j = 0,
\end{aligned} \tag{56}$$

which we can solve for the adjoint power:

$$q^* = -\frac{1}{P_U} \int_U \left[\left(\overline{A} N\right)^T N^* + \sum_{i=0}^{N_j} \mu_j \phi_j \right] d\mathbf{r}, \tag{57}$$

where subscripts U and C represent the unconstrained and constrained regions respectively. Note that the constrained regions do not contribute to the adjoint power whatsoever, and that the jump parameter magnitude can directly influence the adjoint power

magnitude. With q^* evaluated by Eq. (57), the Fredholm alternative will be satisfied and the adjoint diffusion equation will have a non-trivial solution.

With the jump conditions, the inequality constraint multiplier, and the adjoint power fully defined, we may build the adjoint source and perform the E-L calculation.

III.A.4. Flux Filtering

A process we call flux filtering is necessary during the outer iterations due to the numerical nature of the problem. The solution to the inhomogeneous adjoint diffusion equation will contain both homogeneous and particular components:

$$\phi_c^* = \phi_p^* + \alpha\phi_h^*, \tag{58}$$

for any arbitrary scalar α. In such problems, the magnitude of the homogeneous component can become arbitrarily large yet still satisfy the differential equation. Since DIF3D uses regular splitting with the power iteration method to solve the problem rather than direct inversion, the adjoint flux solution becomes contaminated by the homogeneous mode. We modified DIF3D to filter out this contamination guided by the Fredholm alternative condition.

For any arbitrary α, the homogeneous component will satisfy:

$$\left(L^* - k^{-1}B^*\right)\alpha\phi_h^* = 0. \tag{59}$$

Thus, the particular solution will contain all of the information of the adjoint source:

$$S^* = \left(L^* - k^{-1}B^*\right)\left(\alpha\phi_h^* + \phi_p^*\right) = \left(L^* - k^{-1}B^*\right)\phi_p^*. \tag{60}$$

The DIF3D inhomogeneous source iteration with operator splitting proceeds as:

$$\begin{aligned} S^* &= L^*\phi^*_{p,1} \\ S^* + k^{-1}B^*\phi^*_{p,1} &= L^*\phi^*_{p,2} \\ &\vdots \\ S^* + k^{-1}B^*\phi^*_{p,n-1} &= L^*\phi^*_{p,n}. \end{aligned} \tag{61}$$

By forcing $\langle \phi, S^* \rangle = 0$, we step through this iteration using the properties of the adjoint operator:

$$\begin{aligned} \langle \phi, S^* \rangle &= \left\langle \phi, L^*\phi^*_{p,1} \right\rangle = \left\langle \phi^*_{p,1}, L\phi \right\rangle = k^{-1} \left\langle \phi^*_{p,1}, B\phi \right\rangle = k^{-1} \left\langle \phi, B^*\phi^*_{p,1} \right\rangle = 0, \\ k^{-1} \left\langle \phi, B^*\phi^*_{p,1} \right\rangle &= k^{-1} \left\langle \phi, L^*\phi^*_{p,2} - S^* \right\rangle = k^{-1} \left\langle \phi, L^*\phi^*_{p,2} \right\rangle \\ &= \left\langle \phi^*_{p,2}, L\phi \right\rangle = k^{-1} \left\langle \phi^*_{p,2}, B\phi \right\rangle = k^{-1} \left\langle \phi, B^*\phi^*_{p,2} \right\rangle = 0. \end{aligned} \tag{62}$$

Observing that at any step of the iteration, the fission source is orthogonal to the forward flux:

$$\left\langle \phi, B^*\phi^*_{p,i} \right\rangle = 0, \tag{63}$$

we can uniquely determine the parameter α to filter out the contaminating homogeneous component. To do so, we recognize that the contaminated fission source term also has the two components:

$$B^*\phi^*_{c,i} = \alpha B^*\phi^*_{h,i} + B^*\phi^*_{p,i}. \tag{64}$$

Then, we take the inner product with the forward flux and solve for α:

$$\begin{aligned} \left\langle \phi, B^*\phi^*_{p,i} \right\rangle &= \left\langle \phi, B^*\phi^*_{c,i} - \alpha B^*\phi^*_h \right\rangle, \\ 0 &= \left\langle \phi, B^*\phi^*_{c,i} \right\rangle - \alpha \left\langle \phi, B^*\phi^*_h \right\rangle, \\ \alpha &= \frac{\left\langle \phi, B^*\phi^*_{c,i} \right\rangle}{\left\langle \phi, B^*\phi^*_h \right\rangle}. \end{aligned} \tag{65}$$

To ensure a converged solution, the modified DIF3D filters out the contamination at each outer iteration:

$$\phi_{p,i}^{*} = \phi_{c,i}^{*} - \frac{\left\langle \phi, B^{*}\phi_{c,i}^{*} \right\rangle}{\left\langle \phi, B^{*}\phi_{h}^{*} \right\rangle}\phi_{h}^{*}. \tag{66}$$

The filtering process adds slightly to the computational requirements of the optimization algorithm, as it necessitates homogeneous adjoint flux calculations at each time step.

III.A.5. The Terminal Condition

For a reactivity swing objective function, the terminal condition on the E-L equations from Eq. (25) is:

$$N^{*}\left(\mathbf{r},\tau\right) = \frac{\partial}{\partial N}\left[k\left(\tau\right) - k\left(t_{0}\right)\right]. \tag{67}$$

As calculating k requires full lattice physics and global diffusion simulations, evaluating this expression rigorously for each nuclide in each region at BOC and at EOC would be extremely computationally intensive, or would require a depletion perturbation theory method[19]. To avoid complication, we approximate this condition by assuming constant leakage and using k_{∞} rather than k. The condition becomes a function of the collapsed one-group infinite-medium multiplication factor:

$$k\left(t\right) \approx k_{\infty}\left(t\right) = \frac{1}{V}\sum_{r=1}^{R} v_{r}\frac{A\left(\mathbf{r},t\right)}{B\left(\mathbf{r},t\right)} = \frac{1}{V}\sum_{r=1}^{R} v_{r}\frac{\sum_{i=1}^{I}\sum_{g=1}^{G}\nu\sigma_{f,g}^{i}\phi_{g}\left(\mathbf{r},t\right)N_{i}\left(\mathbf{r},t\right)}{\sum_{i=1}^{I}\sum_{g=1}^{G}\sigma_{a,g}^{i}\phi_{g}\left(\mathbf{r},t\right)N_{i}\left(\mathbf{r},t\right)}, \tag{68}$$

where

R is the number of regions in the reactor,

I is the number of nuclides in the system, and

v_{r} is the volume of region r.

From Eq. (68), we can quickly evaluate the terminal condition using our existing

collapsed multi-group cross sections and using standard differentiation rules:

$$\begin{aligned} N_i^*(\mathbf{r},\tau) &\approx \frac{\partial}{\partial N_i}\left[\frac{A(\mathbf{r},\tau)}{B(\mathbf{r},\tau)} - \frac{A(\mathbf{r},t_0)}{B(\mathbf{r},t_0)}\right] \\ &= \left[\frac{\sum_{g=1}^{G}\nu\sigma_{f,g}^i\phi(\mathbf{r},\tau)}{B(\mathbf{r},\tau)} - \frac{A^2(\mathbf{r},\tau)}{B(\mathbf{r},\tau)}\sum_{g=1}^{G}\sigma_a^i\phi_g(\mathbf{r},\tau)\right] \\ &- \left[\frac{\sum_{g=1}^{G}\nu\sigma_{f,g}^i\phi(\mathbf{r},0)}{B(\mathbf{r},0)} - \frac{A^2(\mathbf{r},0)}{B(\mathbf{r},0)}\sum_{g=1}^{G}\sigma_a^i\phi_g(\mathbf{r},0)\right]. \end{aligned} \tag{69}$$

This approximation allows us to set the adjoint number densities for each region at end of cycle. We present the estimated k_∞ values for each case along with the calculated k_{eff} values in the Sec. IV.

III.B. The Adjoint Depletion Equation

Since terminal conditions of the Lagrange multipliers are imposed, we solve the E-L system backwards in time. We do so in a quasi-static fashion, performing explicit finite differencing to determine the derivative of each adjoint nuclide density from Eq. (33). Since $\overline{\eta}$ varies between constrained and unconstrained regions, we compute the adjoint number density derivatives accordingly:

$$\frac{\partial N_i^*}{\partial t} = \begin{cases} -\sum_{g=1}^{G}\phi_g\phi_g^*\left(\frac{\nu\sigma_{f,g}}{k} - \sigma_{a,g}\right) - \sum_{g=1}^{G}\kappa\sigma_{f,g}\phi_g q^* + \sum_{g=1}^{G}N_i^*\sigma_{a,g}^i\phi_g & \text{Unconstrained Regions} \\ -\sum_{g=1}^{G}\phi_g\phi_g^*\left(\frac{\nu\sigma_{f,g}}{k} - \sigma_{a,g}\right) + 2\sum_{g=1}^{G}N_i^*\sigma_{a,g}^i\phi_g. & \text{Constrained Regions} \end{cases} \tag{70}$$

where we have neglected nuclide transitions and radioactive decay terms in the burn matrix.

Thus, with constant real and adjoint flux values, adjoint nuclides deplete at varying rates depending on whether or not they exist in a constrained region. As mentioned

in Sec. II.B., the adjoint densities may become negative. We built the simple adjoint depletion routines directly into DIF3D.

III.C. Search Directions

With the E-L equations uniquely solved, we use the optimality condition to update the control. As discussed in Sec. II.D., we use $\frac{\partial H}{\partial u}$ as a switching function to build search directions for line searches. Control values are updated in proportion with their corresponding search direction magnitude. Only the relative magnitudes of search directions are carried into line searches.

III.D. Line Searching and Backwards Diffusion Theory

We have implemented several levels of rather simple line searching. In each level, search directions for each region are binned into a coarse-mesh histogram. The bins are then translated evenly into a control range. In the TRU enrichment line search, REBUS enrichment modification factors are chosen based on this range. In the BP search, line searches alternate between broadening assembly-to-assembly BP distribution fractions and increasing the total available BP inventory. After each step, the algorithm checks the objective function value and decides between taking an additional step and quitting.

None of the line searches consider the power peaking inequality, so it is possible that a line search step that improves the objective function would cause a violation at some point during the cycle. To properly avoid this, new search directions should be computed at each control update. Under this practice, line searching would be inapplicable, and the computational run-time of the optimization package would grow significantly. Considering this difficulty, we allow the line searches to run unchecked and use a simplified BDT step to eliminate any possible violations[7]. Using BDT we choose decreased flux values at violated regions to satisfy the inequality constraint and solve the diffusion equation backwards, finding the required cross sections of neutron poison in those locations. This solution allows the optimization algorithm to perform efficient line searches on the search

directions and quickly reach an optimal configuration.

IV. REPRESENTATIVE SFR OPTIMIZATION TESTS

Applying the optimization theory discussed, we have systematically optimized fast reactor TRU loadings for three representative SFR configurations with reactivity swing minimization. Common core parameters are listed in Table 1 and optimization performance for all three cases is summarized in Table 2.

IV.A. Case 1 – Homogeneous, Bare Core

The first case is a bare, homogeneous, 0.6 m tall core with no axial reflectors. The first nine radial rings (217 assemblies) are filled completely with fuel. The tenth and eleventh are reflector rings. The outer rings are all shields. High peaking factors are expected in this case due to the high leakage. The original REBUS criticality search set the TRU enrichment of the metallic U-TRU-Zr fuel to 29.1%. The relative radial power distribution of the unoptimized core is shown in Fig. 4. The first search iteration results in a TRU enrichment search direction that tells us to reduce fissile material content in the inner six rings of the core and increase fissile material in the seventh through ninth radial rings in various concentrations, as seen in Fig. 5. The poison control search directions, shown in Fig. 6, tell us to add burnable poisons to the inner rings, and reduce them in the outer rings. As we are unable to control shields and reflectors, the search directions are zero in these regions. The jump iteration in this case converges on a negative value of the jump parameter μ, which in turn requires that the sense of all resulting search directions be switched.

After running a set of line searches on the core, the objective function and the peaking factor are reduced, but the constraint remains violated, so the BDT routines activate. Their execution results in the much flatter, optimized power distribution seen in Fig. 7. In this case, the values of k_∞ estimated by Eq. (68) for the terminal condition were

1.99 and 1.90 for BOC and EOC respectively, compared with the REBUS-calculated k_{eff} values of 1.05 and 1.00. Such a discrepancy can be expected in this extremely high-leakage core. The critical TRU enrichment for the optimized case is 27.4%. The optimization package performed intuitive fuel loading maneuvers resulting in enhanced performance by all measures.

IV.B. Case 2 – Axially Uniform Core

The second case is based on the moderate burner design[20], with control assemblies and gas expansion modules represented, but with no axial reflectors nor shields, and a 0.6 m active core region. The radial core layout is shown in Fig. 3. With control rod assemblies in place, the fuel density has decreased from case 1, and as a result the critical TRU enrichment is correspondingly higher, at 32.0%. As this case contains 354 fuel assemblies, the radial power fall-off is less dramatic. The competing effects of higher fissile enrichment and a lower radial peaking gradient thus result in an unoptimized peaking factor that is comparable to that of the first case. We present the unoptimized radial power distribution in Fig. 8, where we see it is peaked in the center, as expected for a uniform loading. Estimating the terminal conditions on the Lagrange multipliers, we find k_∞ values of 2.04 and 1.98 compared to 1.03 and 1.00 from REBUS, representing higher leakage when compared to the first case. The calculational loop shown in Fig. 1 creates the search directions shown in Fig. 9, which are then applied to line searches and BDT, finally producing the radial power distribution presented in Fig. 10, and the reduced reactivity swing. We again see the intuitive trend of removing fuel from the center and placing it on the periphery, but this case results in a more complicated search direction shape, with distinct instructions to change the control in varying relative magnitudes. With the unoptimized core violating the constraint, the search direction resulted in a new control that reduced the violation. The optimized critical TRU enrichment has been significantly reduced to 27.5%, resulting in a much lower loading of Pu-239 than in the unoptimized case. The destruction of Pu-239 has therefore also been reduced, a possibly undesirable

effect that requires a multi-objective control approach to rectify.

IV.C. Case 3 – Full Core with axial reflectors

The third case is the moderate burner design[20] with axial reflectors and shields, and the 42 cm active core. The radial layout is again given by Fig. 3. The axial leakage in this case is significantly lower than other cases, and accordingly, the required TRU enrichment is much lower, at 18.7%. The unoptimized radial power distribution shown in Fig. 11 is nearly identical to that of case 2, but the axial reflectors reduce the axial peaking factor F_z enough to bring the overall peaking factor down significantly. Still, the obtained search directions provide a control set that reduces both the reactivity swing and the power peaking factor. The optimized case has a critical enrichment of 17.0%.

V. SUMMARY AND CONCLUSIONS

We have derived and applied an optimal control theory to a sodium-cooled nuclear reactor fuel loading, demonstrating the ability to automatically obtain fuel enrichment patterns that reduce an objective function while directly accounting for a power-peaking inequality constraint. We extended time-domain variational calculus to a partial differential equation system to arrive at necessary conditions for optimality, which we solved in diffusion-depletion state space. Our implementation of the conditions required treatment of discontinuous Lagrange multipliers, estimation of the terminal conditions on the multipliers, and numerical filtration of homogeneous-mode contamination. As our Hamiltonian was a linear function of our control, we applied the calculated search directions using Pontryagin's Maximum Principle in several levels of line searching, including a backward diffusion theory search to account for any possible constraint violations. We have shown the method to perform well on three reactor models, reducing the reactivity swing from 4.0% to 2.5% while reducing F_q from 3.0 to 2.0 in one particular case, and similarly in the others. The method is capable of accepting a variety of objective functions

and controls, extracting search directions from variational techniques without guessing, and efficiently pushing the reactor state towards optimality. This offers advantages in calculational speed and in physical intuition over competing stochastic methods.

The optimality conditions solved in this problem are necessary for optimality, but not sufficient. Therefore, obtained solutions can possibly be improved upon further. Furthermore, since we forced only the integrands of several integral equations to vanish, we expect additional control configurations to satisfy the necessary conditions. To seek out these optimal solutions, one would naturally like to refine the control around the search direction. However, since the objective functional is very expensive to compute, a full-cycle perturbation theory accounting for depletion effects could be applied[19]. If done, one could sweep through the core, slightly changing the control of each assembly in various ways to determine the trends that improve optimality. We would also like to implement the more rigorous transuranic enrichment control to obtain possibly improve the quality of the resulting search directions.

APPENDIX A

We must solve the E-L equations with special boundary conditions at junction points to allow for discontinuities in the adjoint variables. The possible jumps arise by taking perturbations of the augmented objective functional in terms of the differential Lagrange multiplier, $d\eta^* = \overline{\eta}\, dt$. Then, the time-domain form of Eq. (24) is:

$$K^\dagger = \Phi(\tau) + \int_0^\tau \lambda^T \left(f - \frac{dx}{dt} \right) dt + \int_0^\tau S\, d\eta^*. \tag{A-1}$$

Integrating by parts, the E-L equations in this case are:

$$d\lambda + \lambda^T \frac{\partial f}{\partial x} dt + \left(\frac{\partial S}{\partial x} \right)^T d\eta^* = 0. \tag{A-2}$$

Integrating these E-L equations over a junction point at t_1 gives:

$$\lambda\left(t_1^+\right) = \lambda\left(t_1^-\right) - \left[\eta^*\left(t_1^+\right) - \eta^*\left(t_1^-\right)\right]\left(\frac{\partial S}{\partial x}\right)_{t_1}. \tag{A-3}$$

The generalized Kuhn-Tucker theorem guarantees that η^* is non-decreasing, thus:

$$\left[\eta^*\left(t_1^+\right) - \eta^*\left(t_1^-\right)\right] \geq 0, \tag{A-4}$$

and therefore, the Lagrange multipliers may suffer a discontinuity at t_1. We define the jump parameter for the j-th junction point as:

$$\mu_j \equiv \left[\eta^*\left(t_1^+\right) - \eta^*\left(t_1^-\right)\right]\left(\frac{\partial S}{\partial x}\right)_{t_j} \tag{A-5}$$

REFERENCES

[1] C. Tzanos, E. Gyftopoulos, and M. Driscoll, "Optimization of Material Distributions in Fast Reactor Cores", *Nucl. Sci. Eng.* **52**, 84 (1973).

[2] W. Terney and E. Williamson Jr, "The Design of Reload Cores Using Optimal Control Theory", *Nucl. Sci. Eng.* **82**, 260 (1982).

[3] C. Drumm and J. Lee, "Gadolinium Burnable Absorber Optimization by the Method of Conjugate Gradients", *Nucl. Sci. Eng.* **96**, 17 (1987).

[4] L.-M. Wu, *Optimal Burnable Poison Loading Strategy*, PhD thesis, Univ. of Michigan (1990).

[5] D. Jacobson, M. Lele, and J. Speyer, "New Necessary Conditions of Optimality for Control Problems with State-Variable Inequality", *J. Math. Anal. Appl.* **35**, 255 (1971).

[6] R. Sorensen, *Systematic Method for Optimizing Plutonium Transmutation in LWRs*, PhD thesis, Univ. of Michigan (2006).

[7] R. Crowther, Methods of Fuel Management Analysis: An Overview, in *National Topical Meeting on Mathematical Models and Computational Techniques for Analysis of Nuclear Systems*, volume 8 (1973).

[8] M. Jessee and D. Kropaczek, "Coupled Bundle-Core Design Using Fuel Rod Optimization for Boiling Water Reactors", *Nuclear Science and Engineering* **155**, 378 (2007).

[9] M. DeChaine and M. Feltus, "Nuclear Fuel Management Optimization Using Genetic Algorithms", *Nucl. Tech.* **111**, 109 (1995).

[10] M. DeChaine and M. Feltus, "Fuel Management Optimization Using Genetic Algorithms and Expert Knowledge", *Nucl. Sci. Eng.* **124**, 188 (1996).

[11] M. Lele and D. Jacobson, "A Proof of the Convergence of the Kelly–Bryson Penalty Function Technique for State-Constrained Control Problems", *J. Math. Anal. Appl* **26**, 163 (1969).

[12] K. Ogata, *State Space Analysis of Control Systems*, Prentice-Hall (1967).

[13] J. Davis, *Optimizing SFR Transmutation Performance Through Direct Adjoining Control Theory*, PhD thesis, Univ. of Michigan (2007).

[14] K. Derstine, "DIF3D: A Code to Solve One-, Two-, and Three-Dimensional Finite-Difference Diffusion Theory Problems", Technical report, ANL-82-64, Argonne National Laboratory (1984).

[15] A. Olson, "A users guide for the REBUS-PC code, version 1.4.", Technical report, ANL/RERTR/TM-32, Argonne National Laboratory (2002).

[16] B. Toppel, A. Rago, and D. O'Shea, "MC2: A Code to Calculate Multigroup Cross Sections", *USAEC Report ANL-7318, Argonne National Laboratory* (1967).

[17] G. Van Rossum et al., "Python Programming Language", *CWI, Department CST, The Netherlands* (1994).

[18] B. Friedman, *Principles and Techniques of Applied Mathematics*, Wiley (1956).

[19] M. Williams, "Development of Depletion Perturbation Theory for Coupled Neutron/Nuclide Fields", Technical report, ORNL/TM-5958, Oak Ridge National Laboratory (1978).

[20] R. Hill, D. Wade, J. Liaw, and E. Fujita, "Physics studies of weapons plutonium disposition in the IFR closed fuel cycle", *Conference: Topical Meeting on Advances in Reactor Physics* (1994).

LIST OF FIGURES

LIST OF TABLES

Table 1. Reactor data common to all calculations

Assembly Pitch	16.14 cm
Fuel Material	U-TRU-Zr
Cladding	HT-9
Coolant	Na
Driver Fuel	LWR-RG-TRU
Host Fuel	Natural U
Power (MWth)	840
Cycle Length (days)	310

Table 2. Optimization performance in terms of reactivity swing, maximum power peaking factors, and Pu-239 destruction. Unoptimized values, values following a control update, and values following a backwards diffusion theory step are shown for three cases.

		Reactivity Swing (%)	Power Peaking Factor F_q	Pu-239 Destruction (kg)
Case 1	Unoptimized	5.03	2.94	116.3
	After Control Update	4.06	2.15	120.0
	After BDT	3.98	2.00	120.3
Case 2	Unoptimized	4.08	2.98	219.5
	After Control Update	3.14	2.92	130.2
	After BDT	2.53	2.00	131.9
Case 3	Unoptimized	3.03	1.92	32.4
	After Control Update	2.70	1.43	38.4
	After BDT	2.62	1.41	36.9

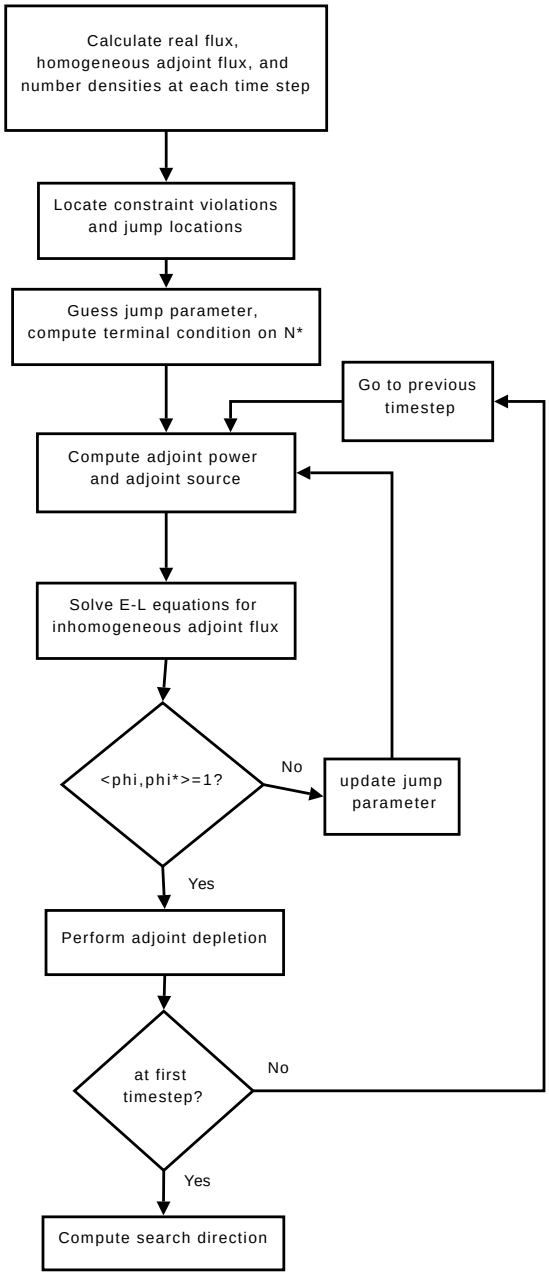

Figure 1. A flowchart showing the computational logic to calculate search directions. Once the forward results are computed, the modified version of DIF3D enters the time-step loop at EOC and proceeds backwards in time to the BOC, performing iterative jump-parameter bisection searches at each time step.

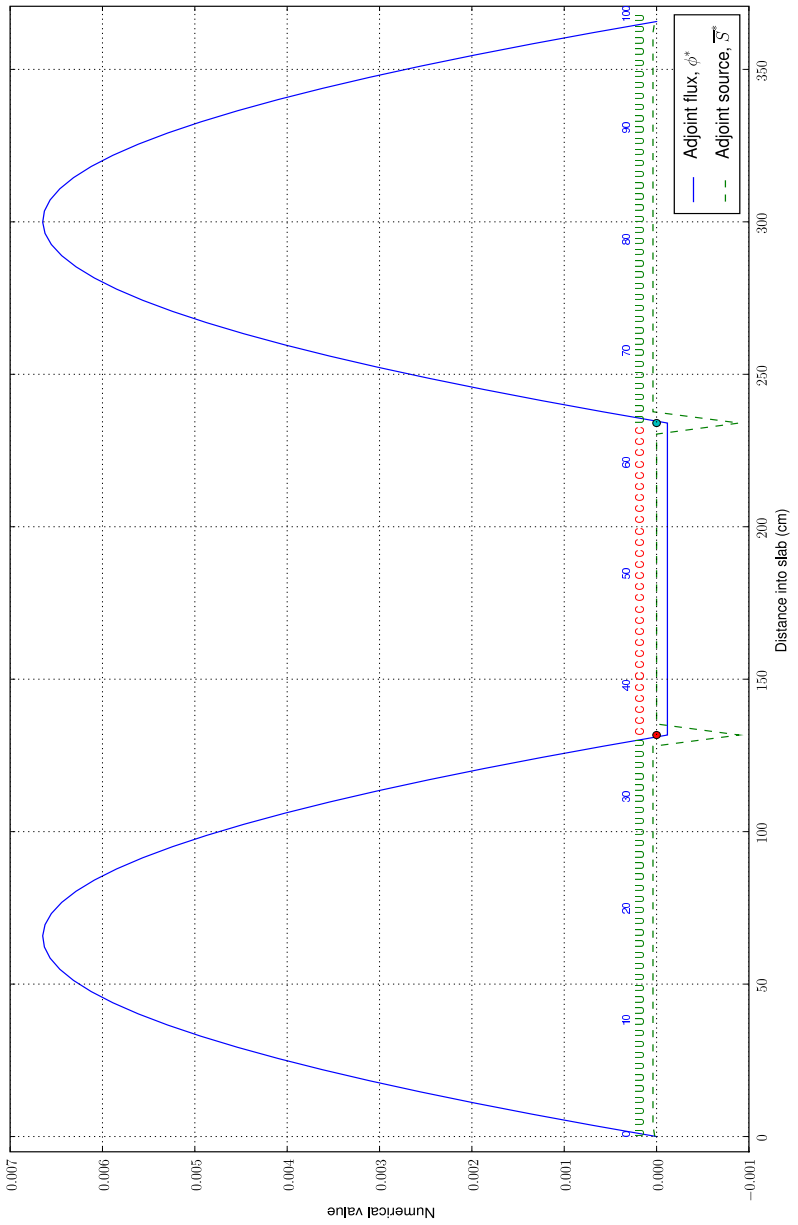

Figure 2. Shape comparison of S^* and ϕ^* in a 1-D homogeneous slab. The Dirac δ-functions used to account for discontinuous adjoint current are visible at the two junction points, where the problem changes from unconstrained (represented by U) to constrained (represented by C).

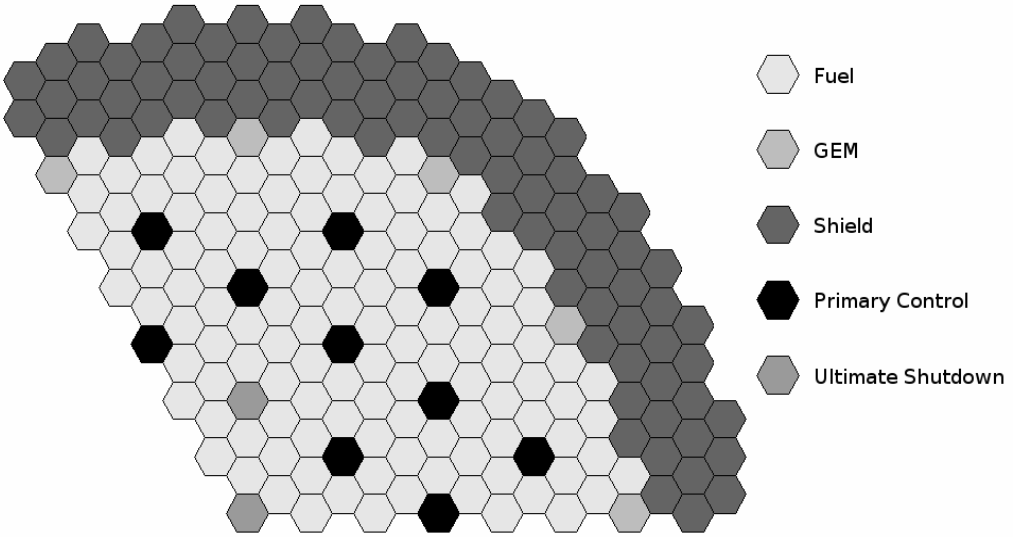

Figure 3. The radial core layout of cases 2 and 3. Control and shutdown systems are withdrawn and gas expansion modules are filled with sodium.

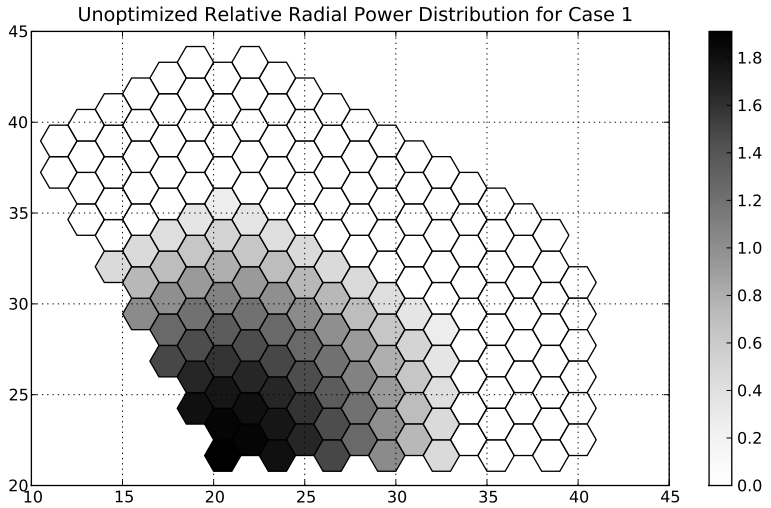

Figure 4. Unoptimized relative radial power distribution for case 1

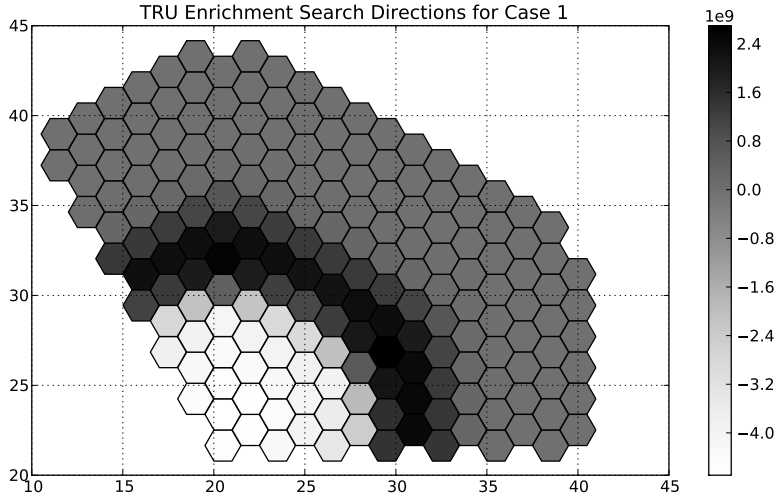

Figure 5. TRU enrichment search directions for case 1

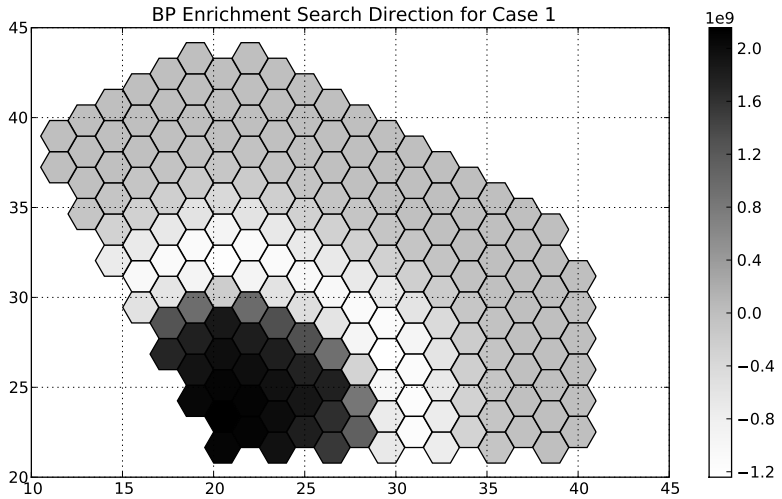

Figure 6. BP enrichment search directions for case 1

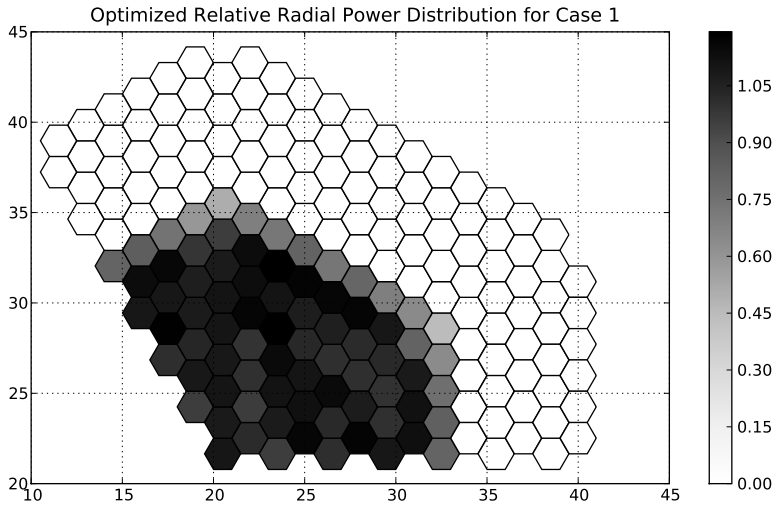

Figure 7. Optimized relative radial power distribution for case 1

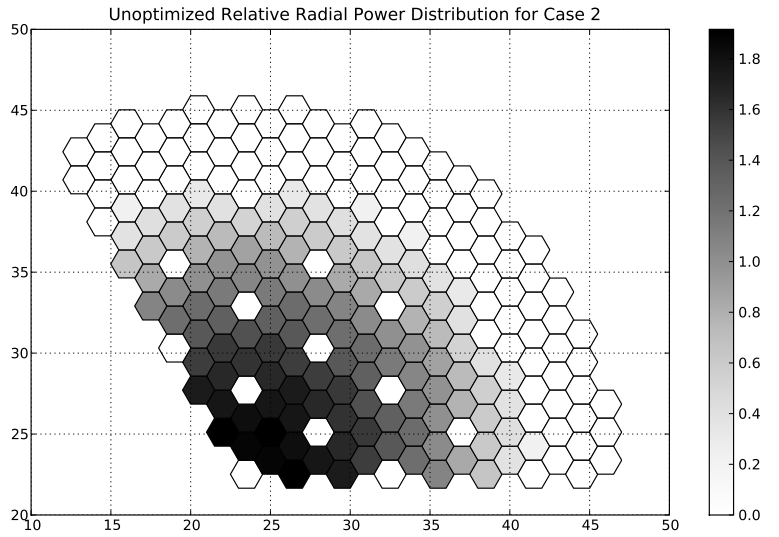

Figure 8. Unoptimized relative radial power distribution for case 2

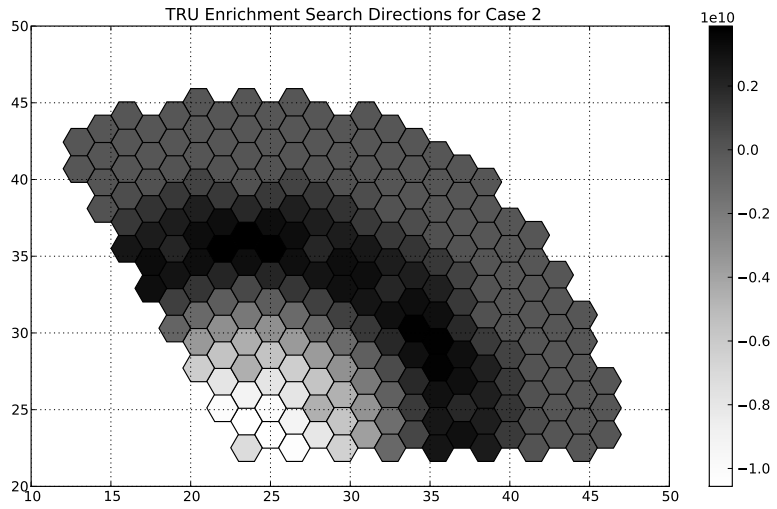

Figure 9. TRU enrichment search directions for case 2

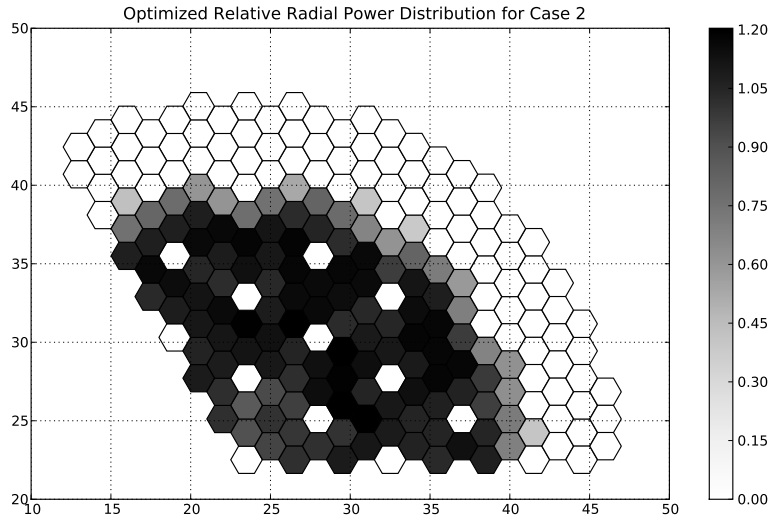

Figure 10. Optimized relative radial power distribution for case 2

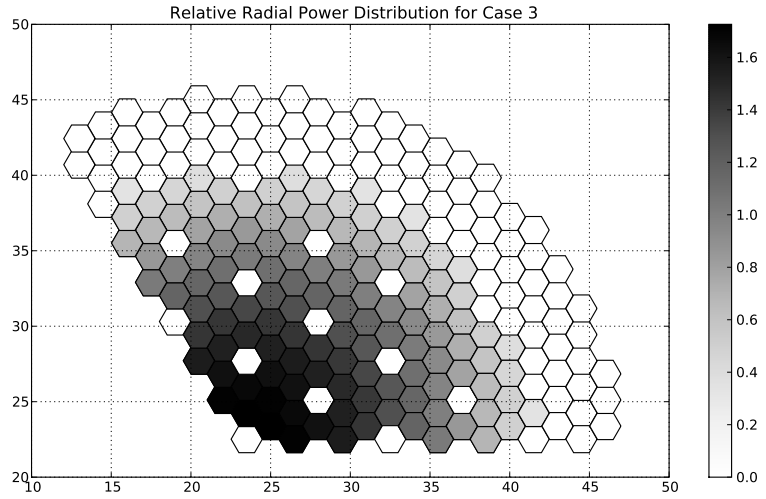

Figure 11. Unoptimized relative radial power distribution for case 3

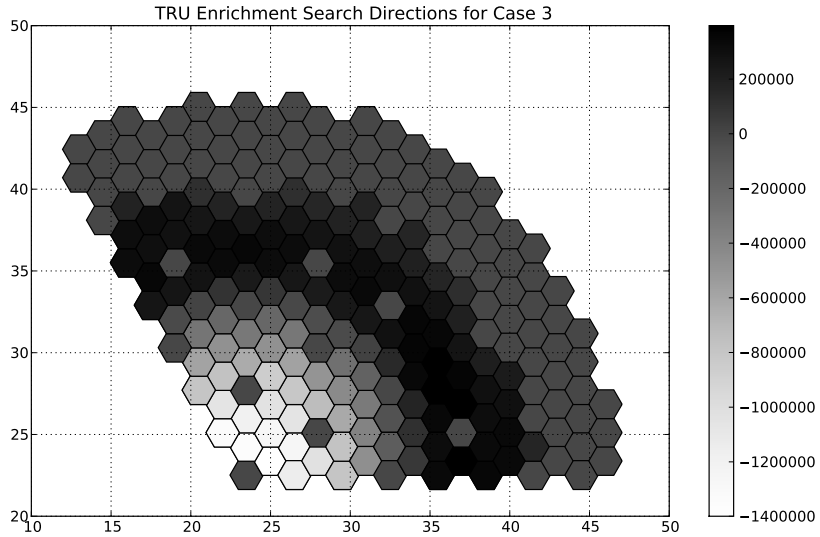

Figure 12. TRU enrichment search directions for case 3

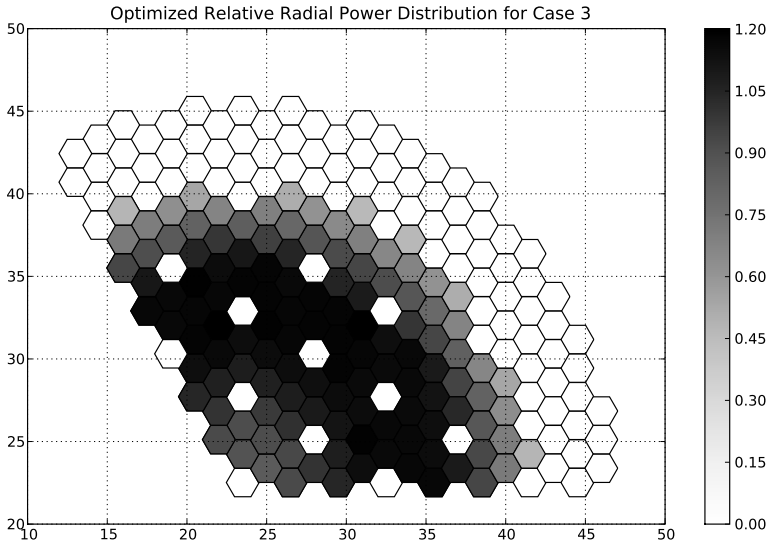

Figure 13. Optimized relative radial power distribution for case 3

Development of a 3-D Global Equilibrium Cycle Methodology for PWRs

William R. Morgan and John C. Lee
Nuclear Engineering and Radiological Sciences
University of Michigan, Ann Arbor, Michigan
wimorgan@umich.edu, jcl@umich.edu

INTRODUCTION

As part of continuing effort to establish light water reactor (LWR) equilibrium cycle search methodology [1,2], we have developed a global equilibrium cycle search algorithm coupling the CPM-3 [3] lattice physics calculations to the 3-D fuel depletion calculations with the PARCS code [4]. The methodology is based on time-dependent microscopic reaction rates extracted from the lattice physics calculations, which are used in global nonlinear isotopic depletion calculations. This allows for efficiently approaching an equilibrium cycle configuration with a fewer number of coupled lattice physics-global depletion calculations than that would be required in direct iterative approach to an equilibrium cycle with an asymptotic burnup map and asymptotic nuclide number densities.

SEARCH ALGORITHM

In searching for an equilibrium cycle, we bypass costly assembly-level calculations by associating operators with incore and excore calculations. The incore fuel cycle accounts for depletion within the reactor, and relates the beginning-of-cycle (BOC) number densities to the end-of-cycle (EOC) number densities. This is accomplished by extracting microscopic reaction rates from the CPM-3 output file to create the transmutation matrix **A**, representing the solution to the isotopic depletion equation:

$$\frac{d\mathbf{N}(t)}{dt} = \mathbf{A}\left[t, \phi(t)\right]\mathbf{N}(t). \qquad (1)$$

Here the matrix **A** contains microscopic cross sections, fluxes, and decay constants, with number density vector **N**(t), representing the CPM-3 21-actinide chain. The solution to this equation is a matrix exponential, which is expanded into a Taylor series

$$\mathbf{N}_d = \prod_{k=1}^{K} e^{\mathbf{A}_k \Delta t_k}\mathbf{N}(0) = \mathbf{B}_{cyc}\mathbf{N}(0) = \mathbf{B}_{cyc}\mathbf{N}_c. \qquad (2)$$

The matrix $\mathbf{B}_{cyc}$ thus relates the charge vector $\mathbf{N}_c$ to the discharge vector $\mathbf{N}_d = \mathbf{N}(\tau)$, with EOC time $\tau = \sum_{k=1}^{K} \Delta t_k$.

To complete the incore fuel depletion algorithm, we need a charge vector $\mathbf{N}_c$ for each assembly, which is accomplished through the excore fuel cycle algorithm. Through this algorithm, we represent the cooling, reprocessing, and reloading of discharged assemblies. For the decay-cooling process, we generate matrix **D** containing all of the decay constants for the 21 nuclides and obtain the decay-cooling matrix **C** for the cooling time period τ_{cool}:

$$\mathbf{C} = e^{\mathbf{D}\tau_{cool}}. \qquad (3)$$

A diagonal reprocessing matrix **R** is then introduced, representing the fraction of each nuclide that is recovered during the reprocessing stage. This reprocessing matrix is combined with the decay-cooling matrix to relate the recovery vector $\mathbf{N}_r$ to the discharge vector $\mathbf{N}_d$:

$$\mathbf{N}_r = \mathbf{RCN}_d \qquad (4)$$

A feed vector $\mathbf{N}_f$, representing an external feed source, is then added to the recovery vector to generate the charge vector for the next cycle:

$$\mathbf{N}_c = \mathbf{N}_r + \mathbf{N}_f = \mathbf{RCN}_d + \mathbf{N}_f, \qquad (5)$$

where $\mathbf{N}_f$ can be chosen according to the recycling strategy.

The equilibrium cycle search begins with CPM-3 calculations for each assembly type. In our study, three different enrichments, 2.0, 2.5, and 3.0 wt%, were used in the first core of the AP600 design [5]. Transmutation matrices **A** are created for each assembly, followed by fuel depletion calculations with the PARCS code. Burnup value for each assembly is converted into EOC time τ, which is used to generate a distinct $\mathbf{B}_{cyc}$ matrix for each assembly, so that EOC number densities can be calculated.

An iterative scheme is then used to search for the next charge vector. A feed vector is chosen based on the recycling and reload pattern selected, with Eqs. (5) and (2) applied until a converged charge vector $\mathbf{N}_c$ is obtained. In the three-batch core we simulate, the discharge vector $\mathbf{N}_d$ represents

the fuel that is discharged from each of the thrice-burned assemblies. These vectors are then averaged, so that charge vector and the recycled fuel in each fresh assembly will be the same.

AP600 EQUILIBRIUM CYCLE

The case we studied is an AP600 core using a self-generated recycling scheme. Here, all plutonium from thrice-burned discharged assemblies is recycled and mixed with 3.5 wt% uranium to create fresh assemblies for reloading.

The main parameter of interest in the equilibrium cycle search is the amount of Pu discharged from thrice-burned assemblies at the end of each cycle. This is summarized in Figure 1, which shows the inventory of Pu discharged per assembly during the search for the equilibrium core. The inventory plots indicate that an equilibrium cycle is attained by the eighth cycle. Each cycle represents typically 5 excore cycle searches via Eqs. (3) and (5).

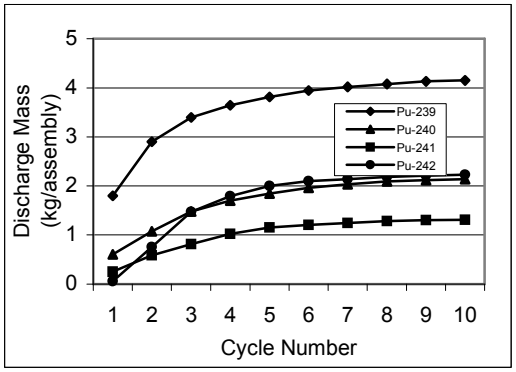

Figure 1. Discharged mass of Pu during the approach to an equilibrium cycle

We also summarize in Table 1 equilibrium cycle characteristics of the core, including BOC isotopic concentrations and a mass balance over the cycle covering U and transuranic (TRU) nuclides. We note that the Pu inventories at the BOC and EOC have converged to ~10 kg/assembly, indicating that an equilibrium cycle is reached

CONCLUSIONS

We have demonstrated the feasibility and efficiency of a 3-D global equilibrium cycle methodology for LWR fuel cycle analyses, which require in general burnup-dependent microscopic reaction rates for a meaningful search for an equilibrium cycle. This is to be contrasted with typical

Table 1. AP600 Equilibrium Cycle Characteristics

Equilibrium Cycle Characteristics		
Cycle Length (EFPD)	420	
^{235}U enrichment (wt%)	3.5	
Pu (wt%) in MOX Fuel	6.81	
Fissile Pu (wt%)	54.4	
Mass Balance		
(kg/assembly)	BOC	EOC
Uranium	458.84	446.52
Neptunium	0.00	0.09
Plutonium	9.99	10.02
Americium	0.00	0.25
Curium	0.00	0.06
Total TRU	9.99	10.42
Total Heavy Metal	468.83	456.94

equilibrium cycle calculations for fast reactors, where a single set of burnup-independent few-group microscopic cross sections may suffice. Our test calculations have been performed to date without explicitly accounting for thermal-hydraulic feedback effects and for burnup-dependent critical soluble boron concentrations. In addition to improving on these approximate treatments in our fuel cycle calculations, additional effort will be required to optimize the fuel loading pattern subject to diverse objective functions.

REFERENCES

1. R. T. Sorensen and J. C. Lee, "LWR Equilibrium Cycle Search Methodology for Assembly-level Fuel Cycle Analysis," *Nucl. Sci. Eng.*, **158**, 213 (2008).
2. R. T. Sorensen and J. C. Lee, "LWR Equilibrium Cycle Search Methodology for Global Fuel Cycle Analysis," *Trans. Am. Nucl. Soc.*, **87**, 332 (2005).
3. D. B. Jones and K. E. Watkins, "CPM-3 Computer Code Manual, Volume 2: User's Manual," EPR-CPM-001-M-002, Revision A, Electric Power Research Institute (2000).
4. H. G. Joo, D. A. Barber, G. Jiang, and T. J. Downar, "PARCS (Purdue Advanced Reactor Core Simulator): A Multi-Dimensional Two-Group Reactor Kinetics Code Based on the Nonlinear Analytic Nodal Method," PU/NE-98-26, Purdue University (1998).
5. "AP600 Standard Safety Analysis Report," DE-AC03-90SF18495, Westinghouse Electric Corporation (1992).

3-D Global Equilibrium Cycle Methodology for PWRs

William R. Morgan and John C. Lee

Department of Nuclear Engineering and Radiological Sciences
University of Michigan, Ann Arbor, MI 48109-2104

Corresponding author: William R. Morgan

Mailing address: Department of Nuclear Engineering and Radiological Sciences
University of Michigan
2355 Bonisteel Blvd
Ann Arbor, MI 48109-2104

Fax: (734) 763-4540
Email: wimorgan@umich.edu

Total number of pages: 18
Number of tables: 2
Number of figures: 10

Abstract

We have developed a global equilibrium cycle search methodology that makes an efficient use of microscopic reactions rates extracted from lattice physics calculations. The piecewise continuous reaction rates are used to solve the isotopic balance equations, approximating lattice physics calculations during the search for an isotopic balance. The solution is iterated with updated microscopic reaction rates until an equilibrium cycle emerges. We have implemented the methodology combining the CPM-3 lattice physics code with the PARCS 3-D diffusion theory code. The equilibrium cycle algorithm has been tested for the AP600 design involving both a self-generated and augmented recycling scheme in CORAIL-type heterogeneous assemblies. In our AP600 test calculations involving two different recycling modes, an equilibrium cycle is attained in 5 and 8 iterations, a small fraction of what would be required for direct calculations.

I. Introduction

The time management of used nuclear fuel (UNF) from light water reactors (LWRs) remains one of the largest problems with operation of nuclear power plants (NPPs). In the next 20 years, the current NPPs will accumulate 87 000 Mg of UNF, in addition to UNF expected from proposed NPPs. Although the Advanced Fuel Cycle Initiative (AFCI) is assessing a number of different reactor technologies for transmutation of UNF, these will not see commercial use until the 2030 timeframe. This suggests the importance of studying ways to utilize the current fleet of LWRs to stabilize the transuranic (TRU) inventory from the UNF stockpile.

In order to best minimize the buildup of TRUs, we must search for an LWR configuration with optimal transmutation capabilities. For this, it is necessary to calculate the equilibrium cycle of such a configuration, which will allow for effective an comparison of TRU destruction capability with different reactor types, include alternate LWR designs and even fast reactors.

As a continuation and extension of R. Sorensen's light water reactor (LWR) equilibrium cycle search methodology [1,2], we have developed a global equilibrium cycle search algorithm coupling the CPM-3 [3] lattice physics calculations to the 3-D fuel depletion calculations with the PARCS code [4]. The methodology is based on time-dependent microscopic reaction rates extracted from the lattice physics calculations, which are used in global nonlinear isotopic depletion calculations. This allows for efficiently approaching an equilibrium cycle configuration with a fewer number of coupled lattice physics-global depletion calculations than that would be required in direct iterative approach to an equilibrium cycle. Sorensen's work focused on the assembly-level methodology, approximating a global equilibrium cycle by using a reactivity-based cycling model [5]. Only preliminary 2-D global equilibrium cycle calculations were reported using the UM2DB code, which is a heavily modified version of the 2DB code [6].

We have implemented a global equilibrium cycle search algorithm coupling CPM-3 and PARCS primarily to establish the feasibility of the algorithm in 3-D global macroscopic depletion calculations. As the first step in developing an equilibrium cycle methodology applicable to general LWR fuel cycle studies, we have performed iterative cycling calculations to obtain an equilibrium core configuration, with the intent to perform the development of optimal fuel loading algorithms in a future study. In this paper, we describe the basic fuel cycle methodology involving the incore and excore fuel cycle algorithms. The incore algorithm develops the method to extract microscopic reaction rates from CPM-3 calculations, while the ex-core algorithm accounts for the decay-cooling, reprocessing, and mixing of fuel feed with discharged fuel. A description of the overall equilibrium cycle search algorithm is then presented, followed by a summary of burnup distributions and Pu inventories obtained in our PARCS equilibrium cycle calculations.

The core configuration for this study is the Westinghouse AP600 reactor, using slightly modified CORAIL assemblies presented in [1]. These are heterogeneous assemblies each containing 198 slightly enriched UO_2 fuel pins with a periphery of 66 MOX fuel pins in a 17×17 array. The initial cycle comprises three batches with 2.0, 2.5, and 3.0 wt% ^{235}U enrichments in a checkerboard pattern. Subsequent cycles use a typical three-batch reload scheme shown in Fig. 1, with 3.5 wt% ^{235}U enrichment for the reload assemblies. Fuel cycle calculations are performed without soluble boron concentration until the end of cycle (EOC) is reached with the effective multiplication factor $k_{eff} = 1.003$.

We begin in Sec. II with a description of the incore fuel cycle algorithm, which extracts reaction rates from the lattice physics code, and uses these to construct an operator that effectively performs a sufficiently accurate fuel depletion calculation over a fuel cycle without repeating lattice physics calculations as fuel isotopics evolve. Section III discusses the excore fuel cycle, where an operator is constructed to simulate cooling

and reprocessing of UNF. In Sec. IV we illustrate the equilibrium cycle search algorithm, primarily the iterative scheme used to arrive at converged feed and discharge number density vectors. Section V explains the two recycling methods used for testing the equilibrium cycle methodology: self-generated Pu recycling and augmented feed Pu recycling. Converged equilibrium cycle results are presented in Sec. VI, followed by a summary and conclusions in Sec. VII.

II. In-Core Fuel Cycle Algorithm

The first step in the incore fuel cycle algorithm is to obtain an operator that relates beginning-of-cycle (BOC) number densities to EOC number densities. This is accomplished by extracting microscopic reaction rates from the CPM-3 output file to create the transmutation matrix $\mathbf{B}_{cyc}$ representing the solution to the isotopic depletion equation:

$$\begin{aligned}\frac{dN_i(t)}{dt} &= \sum_j \left[\sigma_{j\to i}(t)\phi(t) + \lambda_{j\to i}\right] N_j(t) \\ &\quad - \left[\sigma_{ai}(t)\phi(t) + \lambda_i\right] N_i(t), \;\; i = 1,2,\ldots,I, \; j = 1,2,\ldots,I,\end{aligned} \tag{1}$$

where $\sigma_{j\to i}(t)\phi(t)$ and $\lambda_{j\to i}$ are the transmutation rate and a sum of the radioactive decay and (n,2n) reaction rate, respectively, that lead to the production of nuclide *i* from nuclide *j*, while $\sigma_{ai}(t)\phi(t)$ and λ_i are the absorption rate and decay constant for nuclide *i*, respectively. With the CPM-3 21-actinide chain summarized in Fig. 2, Eq. (1) may be set into vector form:

$$\frac{d\mathbf{N}(t)}{dt} = \mathbf{A}\left[t, \phi(t)\right]\mathbf{N}(t), \tag{2}$$

in terms of the nuclear density vector $\mathbf{N}(t) = \left[N_i(t), N_2(t), \ldots, N_I(t)\right]$.

With time steps $\Delta t_k, k = 1,\ldots,K,$ the solution to the isotopic depletion equation (1) is written for the EOC nuclear density vector at $t = \tau$:

$$\mathbf{N}_d = \mathbf{N}(\tau) = \prod_{k=1}^{K} e^{\mathbf{A}_k \Delta t_k}\mathbf{N}(t_0) = \mathbf{B}_{\mathbf{cyc}}\mathbf{N}(t_0) = \mathbf{B}_{\mathbf{cyc}}\mathbf{N}_c; \tau = \sum_{k=1}^{N} \Delta t_k \,. \tag{3}$$

The transmutation matrix $\mathbf{B}_{cyc}$ acts as a single operator that relates the charge vector $\mathbf{N}_c$ at the beginning of cycle (BOC) $t = t_0$ to the discharge vector $\mathbf{N}_d$ at the end of cycle (EOC) $t = \tau$. For the AP600 core design used in the current study, there are three different assembly types, with each type having its own sequence of reaction rate matrices $\mathbf{A}_k$. In global depletion calculations performed with the PARCS code, however, a different EOC burnup is obtained for each individual assembly reflecting a different power density for each assembly. The EOC assembly burnup value is then converted into the EOC time τ_ℓ for assembly ℓ, $\ell = 1,\ldots,L$, and substituted into Eq. (3), so that each assembly has its own unique discharge vector $\mathbf{N}_d$.

III. Ex-core Fuel Cycle Analysis

To complete the in-core fuel depletion algorithm presented in Section II, we need a charge vector $\mathbf{N}_c$ for each assembly, which is accomplished through the ex-core fuel cycle algorithm. Through this algorithm, we represent the cooling, reprocessing, and reloading of discharged assemblies.

For the decay-cooling process, we generate matrix $\mathbf{D}$ containing all of the decay constants for the 21 nuclides and obtain the decay-cooling matrix $\mathbf{C}$ for the cooling time period τ_{cool}:

$$\mathbf{C} = e^{\mathbf{D}\tau_{cool}}. \tag{4}$$

A diagonal reprocessing matrix $\mathbf{R}$ is then introduced, comprising recovery factors r_i, $i = 1,\ldots,I$, giving the fraction of each nuclide that is recovered during the reprocessing stage. This reprocessing matrix is combined with the decay-cooling matrix to relate the recovery vector $\mathbf{N}_r$ to the discharge vector $\mathbf{N}_d$:

$$\mathbf{N}_r = \mathbf{RCN}_d. \tag{5}$$

A feed vector $\mathbf{N}_f$, representing an external feed source, is then added to the recovery vector to generate the charge vector for the next cycle:

$$\mathbf{N}_c = \mathbf{N}_r + \mathbf{N}_f = \mathbf{RCN}_d + \mathbf{N}_f, \tag{6}$$

where $\mathbf{N}_f$ can be chosen according to the recycling strategy. Material flow using these equations is shown in Fig. 3, with ovals depicting mass inventories and rectangles representing fuel cycle operations.

IV. Equilibrium Search Algorithm

The equilibrium cycle search begins with CPM-3 calculations for each assembly type. In our study, three different enrichments, 2.0, 2.5, and 3.0 wt%, were used in the first core. Macroscopic cross section files are generated via a cross section processing program, *macrolinx.f*, in a format readable by PARCS. At this point, **A** matrices in Eq. (2) are also generated for each assembly type, and BOC number densities for each assembly are saved as well. A fuel depletion calculation is then performed with the PARCS code until $k_{eff} = 1.003$ and the burnup value for each assembly is converted into EOC time τ_ℓ. These EOC times are used to generate a distinct $\mathbf{B}_{cyc}$ matrix for each assembly, so that EOC number densities can be calculated.

Once the first cycle is completed, an iterative scheme is used to search for the next charge vector. A feed vector is chosen based on the recycling and reload pattern used, with Eqs. (6) and (3) applied until a converged charge vector $\mathbf{N}_c$ is obtained. In the three-batch core we simulate, the discharge vector $\mathbf{N}_d$ represents the fuel that is discharged from each of the thrice-burned assemblies. These vectors are then averaged, so that charge vector and the recycled fuel in each fresh assembly will be the same. This entire process is shown in Fig. 3.

The algorithm contains two iterative loops, as illustrated in Fig. 4. The innermost loop of the application is described by Eqs. (3) through (6), and constructs in-core and ex-core operators using the reaction rates extracted from CPM-3 calculations. Repeated application of these operators effectively simulates lattice physics calculations, whereby converged charge and discharge vectors are obtained. These converged vectors are

number densities that represent an equilibrium cycle for the specific reaction rates from the previous lattice physics calculation. The algorithm then proceeds to the outer iterative loop, where new reaction rates are obtained using the updated number densities. Once both the inner and outer loops are converged, a true equilibrium cycle has been reached.

Assemblies were loaded using a simple three-batch pattern and a PARCS depletion calculation was performed to reach EOC. All thrice-burned assemblies were removed, with a new feed vector used for creation of fresh assemblies.

V. Recycling Modes

In testing and validating our equilibrium search algorithm, we make use of two different recycling schemes: self-generated Pu (SGP) recycling mode and augmented-feed Pu (AFP) recycling mode. Assemblies were loaded using a simple three-batch pattern and a PARCS depletion calculation was performed to reach EOC. We represent a typical three-batch core with a total discharge burnup of 42~45 MWd/kgHM. Once the target batch-average burnup is achieved, the thrice-burned assemblies are discharged and allowed a cooling period of 5 years, after which they undergo reprocessing and refabrication. In the SGP mode, all self-generated Pu is recycled. The remaining fuel mass is composed of enriched U, the enrichment of which can be adjusted to obtain the desired cycle length.

Alternatively, the AFP recycling mode does not involve the recycling of any of the UNF in the assemblies. It instead utilizes a Pu feed vector, representing the average composition which will be accumulated in France by 2016. This feed vector gives the isotopic weight percents as {^{238}Pu, ^{239}Pu, ^{240}Pu, ^{241}Pu, ^{242}Pu | 0.027, 0.56, 0.259, 0.081, 0.073}. The remainder of the fuel is U at a fixed enrichment.

VI. Equilibrium Cycle Results

The first parameter of interest in the equilibrium cycle search is the amount of Pu discharged from thrice-burned assemblies at the end of each cycle. This is summarized

in Figures 5 and 6, which show the inventories of Pu discharged per assembly during the search for the equilibrium core, with an equilibrium cycle length of 420 equivalent full power days (EFPDs) for SGP recycling mode, and 450 EFPDs for AFP recycling mode. These cycle lengths are calculated from PARCS output, at the point when $k_{eff} = 1.003$. The inventory plots indicate that an equilibrium cycle is attained by the eighth cycle. Each cycle represents typically 5 ex-core cycle searches via Eq. (6).

In the approach to equilibrium, fewer calculations were required to obtain converged number densities for AFP recycling than for SGP. This is due to the external feed of Pu for AFP, which causes the fractional change in TRUs to be less as we approach an equilibrium cycle. Since the smaller fractional changes in number densities mean that reaction rates will be similar for subsequent cycles, the AFP case apparently converges faster to an equilibrium cycle.

Assembly-wise burnup distributions at the BOC and EOC are also of interest when examining an equilibrium cycle. Figures 7 and 8 show the equilibrium BOC burnup distributions and normalized assembly power maps for a quarter core, while Figs. 9 and 10 show the corresponding EOC burnup distributions and power maps. In both cases, we see the expected flattening of power across the core as the cycle progresses, with similar assembly-wide power and burnup maps.

Finally, we summarize equilibrium cycle characteristics of the core, including BOC isotopic concentrations and a mass balance over the cycle covering U and TRU nuclides in Tables 1 and 2. We note that the Pu inventories at the BOC and EOC have converged to ~10 kg/assembly for the SGP recycling, whereas they are converged to ~17 kg/assembly for AFP recycling, indicating that equilibrium cycles are reached for each case. Both an increased Pu content and the higher concentration of fissile Pu in the AFP case lead to a spectral hardening of the flux, seen in the larger fast-to-thermal flux ratios. This spectral shift also leads to a lower reactivity swing, as the absorption of neutrons in

^{238}U leads to the production of ^{239}Pu which is more likely to undergo fission in the harder spectrum. This is also true in the production of fertile TRUs.

VII. Summary and Conclusions

In our effort to develop an equilibrium cycle methodology for global LWR fuel cycle analysis, we have coupled the CPM-3 lattice physics code with the PARCS 3-D diffusion theory code for a demonstration of the methodology. Our test cases are three-batch AP600 configurations involving either the recycling of all self-generated Pu, or a feed vector composed of stockpiled Pu, both in a CORAIL-type heterogeneous assembly design. Through the use of microscopic reactions rates extracted from CPM-3 depletion calculations, we are able to arrive at a balanced ex-core cycle for each set of lattice physics calculations and the corresponding macroscopic cross section libraries. Once the ex-core nuclide balance is satisfied, we perform a new set of CPM-3 calculations to update the microscopic reaction rates. This process is repeated for a fixed fuel loading pattern to arrive at an equilibrium cycle.

We have demonstrated the feasibility and efficiency of a 3-D global equilibrium cycle methodology for LWR fuel cycle analyses, which require in general burnup-dependent microscopic reaction rates for a meaningful search for an equilibrium cycle. This is to be contrasted with typical equilibrium cycle calculations for fast reactors, where a single set of burnup-independent few-group microscopic cross sections may suffice. Our test calculations have been performed to date without explicitly accounting for thermal-hydraulic feedback effects and for burnup-dependent critical soluble boron concentrations. In addition to improving on these approximate treatments in our fuel cycle calculations, additional effort will be required to optimize the fuel loading pattern subject to diverse objective functions. Further effort is also required to streamline our equilibrium cycle methodology so that it may be applied with alternate lattice physics codes.

References

1. R. T. Sorensen and J. C. Lee, "LWR Equilibrium Cycle Search Methodology for Assembly-level Fuel Cycle Analysis," *Nucl. Sci. Eng.*, **158**, 213 (2008).

2. R. T. Sorensen and J. C. Lee, "LWR Equilibrium Cycle Search Methodology for Global Fuel Cycle Analysis," *Trans. Am. Nucl. Soc.*, **87**, 332 (2005).

3. D. B. Jones and K. E. Watkins, "CPM-3 Computer Code Manual, Volume 2: User's Manual," EPR-CPM-001-M-002, Revision A, Electric Power Research Institute (2000).

4. H. G. Joo, D. A. Barber, G. Jiang, and T. J. Downar, "PARCS (Purdue Advanced Reactor Core Simulator): A Multi-Dimensional Two-Group Reactor Kinetics Code Based on the Nonlinear Analytic Nodal Method," PU/NE-98-26, Purdue University (1998).

5. M. J. Driscoll and T. J. Downar, *Linear Reactivity Model*, American Nuclear Society (1989).

6. W. W. Little Jr. and R. W. Hardie, "2DB – A Two-Dimensional Fast Reactor Burnup Code," *Nucl. Sci. Eng.*, **32**, 275 (1968).

List of Figures and Tables

3	2	1	2	1	1	3
2	1	2	2	2	1	3
1	2	1	2	1	3	3
2	2	2	1	2	1	3
1	2	1	2	3	3	
1	1	3	1	3		
3	3	3	3			

Batch	Burnup
1	Twice-Burned
2	Once-Burned
3	Fresh Fuel

Figure 1. Fuel loading map for reload cycles

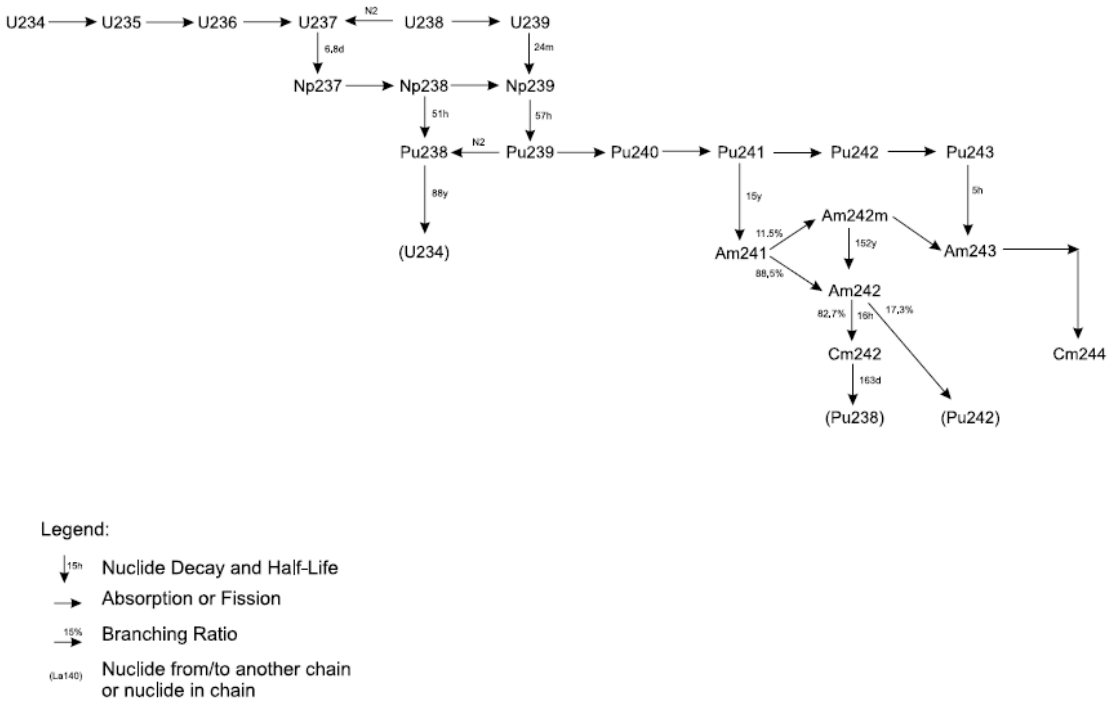

Figure 2. CPM-3 nuclide chain

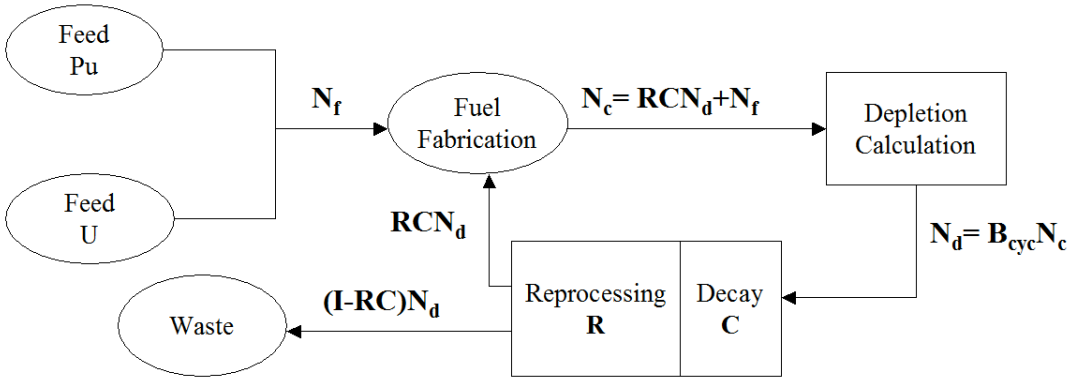

Figure 3. Diagram of material flow for fuel cycle. Here ovals represent mass inventories, while rectangles represent fuel cycle operations

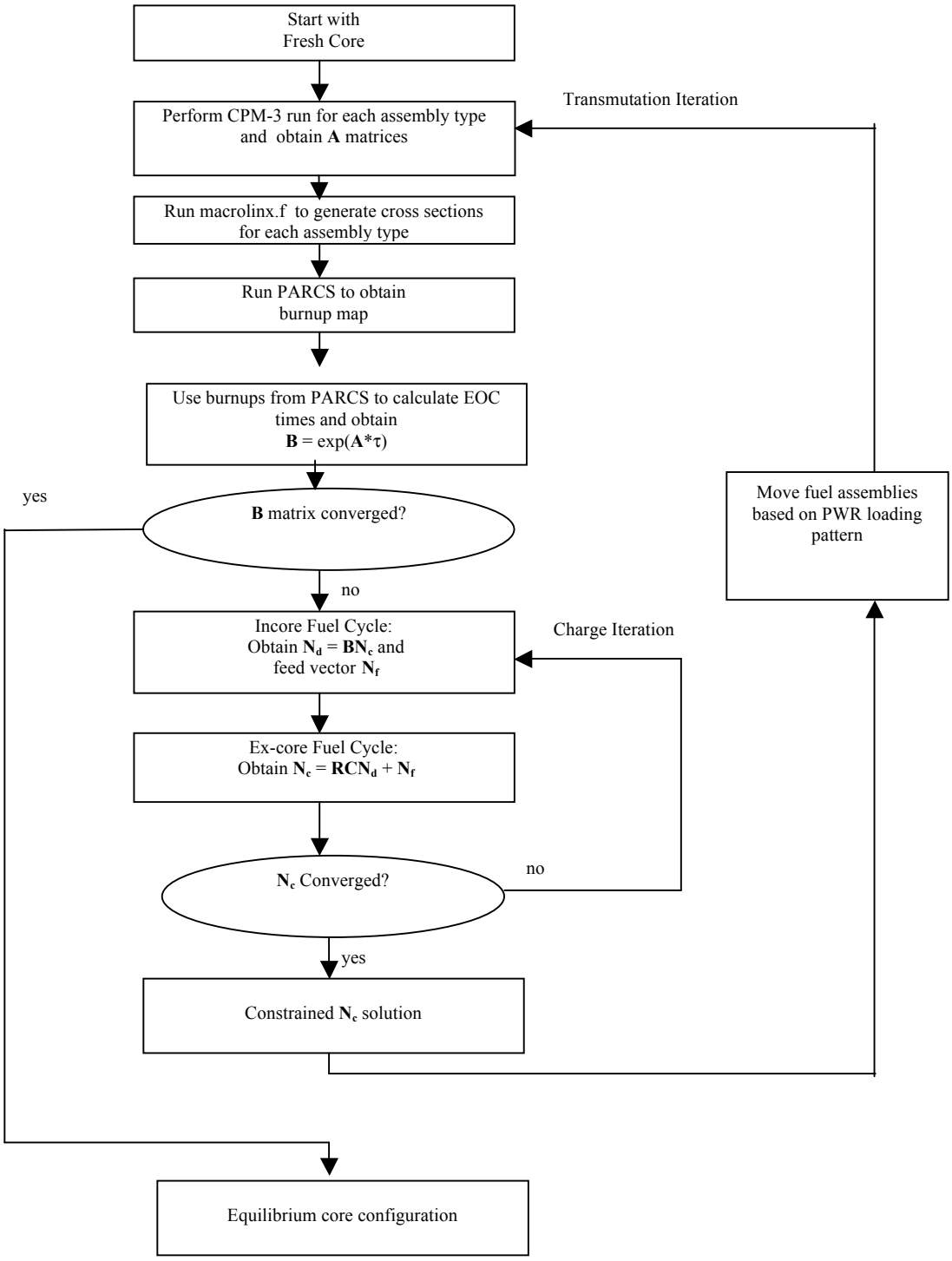

Figure 4. Flow chart for the equilibrium cycle search algorithm

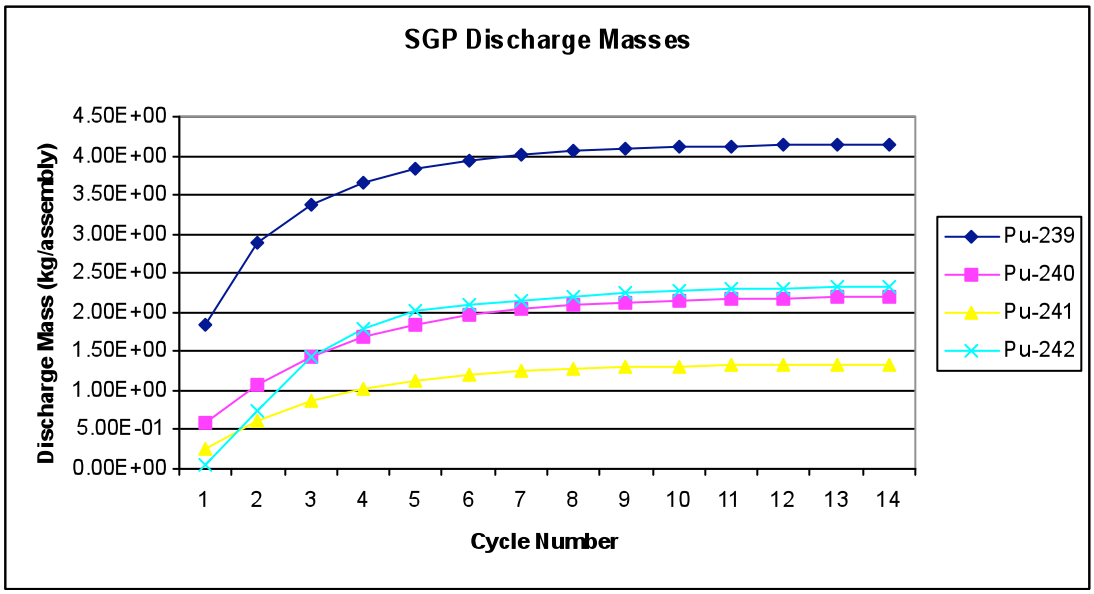

Figure 5. Discharged mass of Pu during the approach to an equilibrium cycle using SGP recycling mode

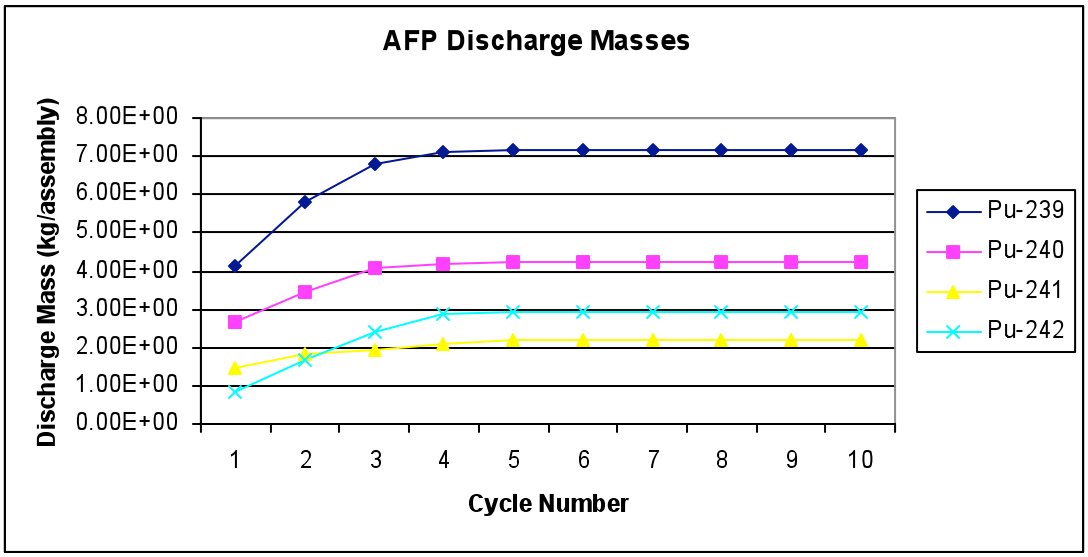

Figure 6. Discharged mass of Pu during the approach to an equilibrium cycle using AFP recycling mode.

Assembly Power Distribution

1.4658	1.1207	0.8867	1.0642	0.9014	0.8355	0.9599
1.1207	0.9025	0.9686	1.1039	1.1230	0.9960	1.0236
0.8867	0.9686	0.9069	1.1179	1.0052	1.3170	1.0392
1.0642	1.1039	1.1179	1.0854	1.0099	0.7958	0.7129
0.9014	1.1230	1.0052	1.0099	1.1808	0.8067	
0.8355	0.9960	1.3170	0.7958	0.8067		
0.9599	1.0236	1.0392	0.7129			

Assembly Burnup Distribution

0.000	11.750	28.681	12.272	28.840	31.795	0.000
11.750	29.135	16.081	12.202	8.776	25.172	0.000
28.681	16.081	29.135	10.141	26.950	0.000	0.000
12.272	12.202	10.141	14.767	19.474	34.311	0.000
28.840	8.776	26.950	19.474	0.000	0.000	
31.795	25.172	0.000	34.311	0.000		
0.000	0.000	0.000	0.000			

Figure 7. BOC burnup distribution (MWd/kgHM) and assembly power map for the equilibrium cycle using the SGP recycling mode.

Assembly Power Distribution

1.4696	1.1250	0.8917	1.0681	0.9078	0.8428	0.9627
1.1250	0.9080	0.9704	1.1065	1.1264	1.0010	1.0250
0.8917	0.9704	0.9095	1.1158	1.0052	1.3156	1.0384
1.0681	1.1065	1.1158	1.0770	0.9985	0.7960	0.7116
0.9078	1.1264	1.0052	0.9985	1.1681	0.8006	
0.8428	1.0010	1.3156	0.7960	0.8006		
0.9627	1.0250	1.0384	0.7116			

Assembly Burnup Distribution

0.000	12.397	29.883	12.918	30.038	32.982	0.000
12.397	30.319	17.046	12.801	9.221	26.248	0.000
29.883	17.046	30.319	10.694	28.136	0.000	0.000
12.918	12.801	10.694	15.638	20.978	35.504	0.000
30.038	9.221	28.136	20.978	0.000	0.000	
32.982	26.248	0.000	35.504	0.000		
0.000	0.000	0.000	0.000			

Figure 8. BOC burnup distribution and assembly power map for the equilibrium cycle using AFP.

Assembly Power Distribution

1.2717	1.1207	0.9660	1.1327	0.9706	0.8778	0.9010
1.1076	0.9547	1.0549	1.1555	1.1547	0.9801	0.9297
0.9660	1.0547	0.9872	1.1654	1.0193	1.1858	0.9209
1.1327	1.1555	1.1654	1.1244	1.0320	0.8031	0.6977
0.9706	1.1547	1.0193	1.0320	1.1146	0.7986	
0.8778	0.9801	1.1858	0.8013	0.7986		
0.9010	0.9297	0.9209	0.6977			

Assembly Burnup Distribution

20.868	29.170	43.275	29.349	42.910	43.953	12.387
29.170	43.745	32.003	29.683	25.766	39.033	12.914
43.275	32.003	43.899	27.594	41.783	17.045	12.812
29.349	29.683	27.594	31.270	34.136	45.284	9.248
42.910	25.766	41.783	34.136	15.741	10.754	
43.953	39.033	17.045	45.284	10.754		
12.387	12.914	12.813	9.248			

Figure 9. EOC burnup distribution and assembly power map for the equilibrium cycle using the SGP recycling mode.

Assembly Power Distribution

1.2658	1.1026	0.9637	1.1297	0.9722	0.8824	0.9046
1.1026	0.9523	1.0501	1.1525	1.1544	0.9833	0.9330
0.9637	1.0501	0.9853	1.1618	1.0191	1.1876	0.9240
1.1297	1.1525	1.1618	1.1195	1.0266	0.8072	0.7017
0.9722	1.1544	1.0191	1.0266	1.1145	0.8019	
0.8824	0.9833	1.1876	0.8072	0.8019		
0.9046	0.9330	0.9240	0.7017			

Assembly Burnup Distribution

22.298	31.029	45.535	31.210	45.176	46.109	13.327
31.029	45.988	34.071	31.515	27.443	41.163	13.878
45.535	34.071	46.142	29.341	44.023	18.272	13.752
31.210	31.515	29.341	33.215	36.562	47.304	9.939
45.176	27.443	44.023	36.562	16.786	11.515	
46.109	41.163	18.272	47.304	11.515		
13.327	13.878	13.752	9.939			

Figure 10. EOC distribution and assembly power map for the equilibrium cycle using AFP.

Table 1. Summary of Equilibrium Cycle Characteristics

Equilibrium Cycle Characteristics				
	SGP		**AFP**	
Cycle Length (EFPD)	420		450	
^{235}U enrichment (wt%)	3.5		4.0	
Pu (wt%) in MOX Fuel	6.81		11.59	
Fissile Pu (wt%)	54.4		64.1	
Mass Balance				
(kg/assembly)	BOC	EOC	BOC	EOC
Uranium	458.84	446.52	454.91	444.68
Neptunium	0	0.09	0	0.72
Plutonium	9.99	10.02	17.06	17.20
Americium	0	0.25	0	1.04
Curium	0	0.06	0	0.46
Total TRU	9.99	10.42	17.06	19.42
Total Heavy Metal	468.83	456.94	471.97	464.10

Table 2. Summary of Equilibrium Cycle Reactor Characteristics

Reactor Characteristics for Equilibrium Cycle		
	SGP	**AFP**
Cycle Reactivity Swing (% Δk/k)	21.4	16.1
Fast-to-Thermal Flux Ratio		
BOC	7.263	7.931
EOC	7.557	8.233
Radial Peaking Factor		
BOC	1.465	1.469
EOC	1.271	1.265
Axial Peaking Factor		
BOC	1.480	1.469
EOC	1.051	1.099